2018

MEASUREMENT OF PLANAR FAULT PROBABILITIES IN AUSTEMPERED DUCTILE IRON AND 304L STAINLESS STEEL

Nathan Peterson
Michigan Technological University, nepeters@mtu.edu

MEASUREMENT OF PLANAR FAULT PROBABILITIES IN AUSTEMPERED DUCTILE IRON AND 304L STAINLESS STEEL

By

Nathan E. Peterson

A THESIS

Submitted in partial fulfillment of the requirements for the degree of

MASTER OF SCIENCE

In Materials Science and Engineering

MICHIGAN TECHNOLOGICAL UNIVERSITY

2018

This thesis has been approved in partial fulfillment of the requirements for the Degree of MASTER OF SCIENCE in Materials Science and Engineering.

Department of Materials Science and Engineering

Thesis Advisor:	*Dr. Paul Sanders*
Committee Member:	*Dr. Edward Laitila*
Committee Member:	*Dr. Daniel Seguin*
Department Chair:	*Dr. Stephen Kampe*

Table of Contents

List of figures

List of tables

Acknowledgements

I'd like to first thank both my advisor Paul Sanders and SINTOKOGIO Japan for sponsoring my degree project and giving me the opportunity to pursue research at the academic level.

I'd also like to thank my committee members, Paul Sanders, Dan Seguin, Edward Laitila along Peter Moran and my future advisor Sean Agnew at UVa for guiding me through the thesis writing process, along with providing insightful knowledge throughout my entire project and helping me to interpret my results concisely.

Finally, I'd like to thank Jonathan Almer at Argonne National Lab for running diffraction experiments on an extremely short notice to help complement my results collected at Michigan Tech.

This research used resources of the Advanced Photon Source, a U.S. Department of Energy (DOE) Office of Science User Facility operated for the DOE Office of Science by Argonne National Laboratory under Contract No. DE-AC02-06CH11357.

Abstract

During plastic deformation both stacking and twin faults can be generated in face-centered cubic materials, including iron-based metals that contain thermally stable austenite. These planar faults are a critical component of the austenite to martensite transformation, forming shear bands that can act as nucleation sites. The measurement of these faults via x-ray diffraction has been long established, however it has not been applied widely to austempered ductile irons. The ability to measure these faulting probabilities could give insights into the transformation as a function of deformation. In this work both planar fault densities were measured in austempered ductile iron to test the feasibility of the x-ray diffraction peak-shift (stacking) and centroid-shift (twin) techniques in these materials using a traditional laboratory diffractometer and synchrotron beamline source. Experimentation was also performed with 304L stainless steel as a baseline material for comparison. The errors associated with this technique are also discussed and highlighted. Errors in the laboratory diffractometer measurement were shown to be significant and therefore the experimental setup should be carefully considered when performing these types of analyses.

1 Background

1.1 FCC to BCC/BCT Martensite Transformation

Certain materials exhibit diffusion-less, massive transformations that are commonly known as a martensite transformation [1]. This type of transformation is the physical explanation for the shape-memory effect in alloys such as, In-Ti or Ni-Ti [2] and is utilized in transformation induced plasticity steels for an increased strain-hardening response [3,4]. In steels, the martensite start, or M_s temperature is a crucial factor to consider when designing heat-treatments for hardening and strengthening of steels. This is the temperature where the metastable austenite transforms to the stable martensite phase, which in steels can be either body-centered cubic (BCC) or body-centered tetragonal (BCT), depending on the carbon content. When the austenite is stabilized through alloying additions, the M_s temperature drops below room temperature, enabling higher amounts of retained austenite at room temperature. As is shown in Figure 1.1, with the increased thermal stability of austenite an additional source of energy is required to start the martensite transformation. This additional energy can be provided via applied strains. Both elastic and plastic strains have been shown to influence this transformation, depending on the additional energy required to start the transformation. Stress-assisted transformations occur with only elastic strains on the material, thus requiring less overall energy than strain-induced transformations, which require plastic deformations to occur. To help characterize these types of steels, the M_d, or temperature at which deformation begins to cause the transformation is introduced to complement the M_s temperature.

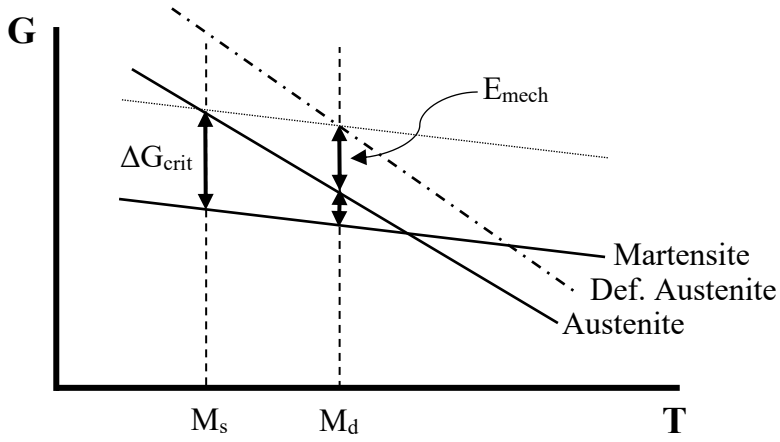

Figure 1.1: G-T diagram of austenite and martensite highlighting the differences in M_s and M_d temperatures. The additional mechanical energy required at M_d is shown as E_{mech}, and the total G required for martensite transformation is shown as ΔG_{crit}. An additional deformed austenite G-T curve is shown as well.

In general, whether thermally or mechanically activated, the martensite transformation has been observed to be a diffusion-less shear (displacive) transformation [1]. The observed orientation relationship between the martensite and austenite boundaries gives the habit plane between the two phases, which has been described by Kurdjumov-Sachs and Bogers-Burgers. From these models, the vectors for the shear required for the transformation has been determined to be $\frac{1}{12}\langle 112\rangle$ for the K-S model and $\frac{1}{18}\langle 112\rangle$ B-B model, which are in the same direction as the Shockley partial dislocation present from a stacking fault as described in Section 1.2.1.[5] This relationship between the Shockley partial and the shear vector from the B-B model is the source of the Olson and Cohen nucleation theory described below. Olson and Cohen theorized that the build-up of stacking faults along with twin faults or ε (HCP) martensite (referred to as shear-bands) act as nucleation sites for the martensite within the austenite grains [6–8]. The general sequence of Olson-Cohen nucleation site theory, is shown in Figure 1.2.

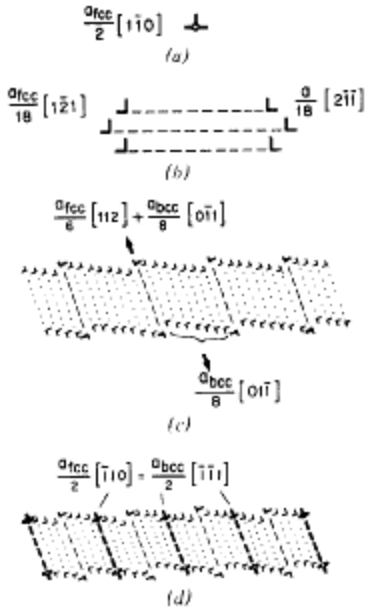

Figure 1.2: Dislocation motion and creation sequence in the Olson-Cohen theory for martensite nucleation in the FCC->BCC transformation. Step a) is the initial Shockley edge dislocation present on a (111) plane in the FCC lattice. B) are the 3 partial dislocations created, where the $1/18\,[\bar{1}2\bar{1}]$ and $1/18\,[\bar{2}11]$ partial dislocations are equivalent to 1/3 of the normal partial $1/6\,[\bar{1}2\bar{1}] + 1/6\,[\bar{2}11]$ dislocations, where they are split onto three consecutive planes. C) is the formation of partial dislocations during the relaxation of the fault in B). D) is the final fault structure after additional lattice screw dislocations are created to relieve the stresses produced during the initial relaxation in C).[1]

Initially, an $\frac{1}{2}[\bar{1}10]$ screw dislocation dissociates on the (111) plane, producing $\frac{1}{18}[\bar{1}2\bar{1}]$ and $\frac{1}{18}[\bar{2}11]$ dislocations on three consecutive planes. As shown in the Bogers-Burgers model in this configuration, the atoms may easily move to the positions in the body centered structure during the transformation sequence [9]. A formalized kinetic model was developed for steels that leverage transformation-induced plasticity that is based on shear-band intersections as nucleation sites [10]. The model assumes that the

[1] Reprinted by permission from Springer Nature: Springer Metallurgical Transactions A, A general mechanism of martensitic nucleation: Part II. FCC → BCC and other martensitic transformations, G. B. Olson, Morris Cohen 1976. See Appendix F for documentation to republish this material.

intersections of the shear bands (stacking faults, twin faults, ε-martensite) increase linearly with the strain applied and that the probability of a certain shear band intersection will nucleate martensite follows a Gaussian distribution. The model, Equation 1.1, contains three variables, α, β and n that must be fitted experimentally to a specific material. The model calculates the fraction of martensite (α') present as a function of strain applied (ε).

$$f_{\alpha'} = 1 - e^{-\beta[1-\exp(-\alpha\varepsilon)]^n} \quad (1.1)$$

The alpha term is dependent on the rate of shear-band formation as a function of applied strain and the beta term is directly related to the probability that a given shear-band intersection will become a martensite nucleation site. The beta term is also dependent on the thermodynamic driving force for transformation ($\Delta G_{\alpha \text{ to } \gamma}$). These terms along with the exponent, *n*, are determined through fitting of experimental data for a given alloy. Based on this theory, the planar fault defects present in materials are a critical component to understand for further understanding of this transformation.

1.2 Planar defects in FCC Materials

Stacking and twin faults can occur during plastic deformation, while twin faulting can also occur during recrystallization from heat treatment. FCC materials undergoing plastic deformation can exhibit either or both deformation modes, dislocation slip or twinning, with dislocation slip producing stacking faults and twinning producing twin faults on the close packed (111) plane [11,12]. During recrystallization, errors in the growth sequence can also cause twin faulting, where the crystal stacking sequence is mirrored around a twin fault. Understanding of the deformation behavior character, whether it is by slip or

by twinning, is important in material design. Examples of materials leveraging a specific deformation mode for enhanced properties include both twinning-induced plasticity (TWIP) and transformation-induced plasticity (TRIP) type high-strength steels. TWIP steels utilize deformation twinning to increase the work-hardening response compared to traditional alloy steels, while TRIP steels utilize dislocation slip (stacking fault generation) to transform the austenite to martensite to increase the work-hardening response compared to traditional alloy steels [4].

1.2.1 Stacking Faults in FCC Materials

A stacking fault is a defect in the normal stacking order of planes in the crystal lattice, that can be created during dislocation slip. In the FCC structure, the close packed plane (111) follows the *ABCABCABCABC* sequence, each letter designating the unique layer of atoms in the crystal as shown in Figure 1.3.

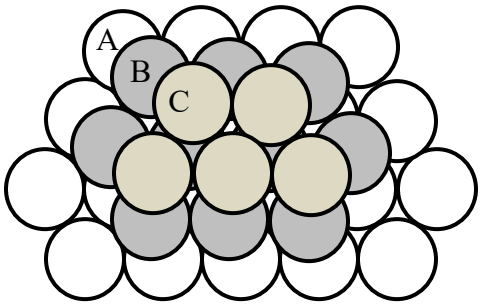

Figure 1.3: 2-dimensional projection of the (111) close packed plane showing the *ABCABC* stacking sequence in an FCC lattice. The individual layers are labeled *A*, *B*, *C* respectively.

Dislocation slip occurs primarily on the close-packed planes in the face-centered cubic structure. During the dislocation slip process, the burgers vector of an edge dislocation in the (111) plane is $\frac{1}{2}[\bar{1}10]$, which follows the direct path to the next *B* site, where the

atoms missing in the *B*-plane correspond to the missing plane from the edge dislocation. This type of motion is depicted in Figure 1.5X. This method of dislocation slip is not the most energetically favorable (less energy) because of the relatively large lattice strains required to move the *B*-layer atoms directly over the *A*-layer atoms to the next *B*-layer position, where this energy is directly proportional to the square of the burgers vector for the dislocation and shear modulus of the material (Gb^2). A more energetically favorable method of this motion is when the edge dislocation is split into two partial dislocations to arrive at this same site on the lattice, as depicted in Figure 1.5. The dislocation disassociates following the relation $\frac{1}{2}[\bar{1}10] = \frac{1}{6}[\bar{1}2\bar{1}] + \frac{1}{6}[\bar{2}11]$, thus moving the atoms to the *C* position after the first partial and returning to the *B* position after the second partial. The b^2 of the partials (0.33) combined is lower than the b^2 required for the edge dislocation (0.5). This partial dislocation sequence is known as the Shockley partial dislocation sequence [1]. This dislocation disassociation sequence is depicted in further detail in Figure 1.4.

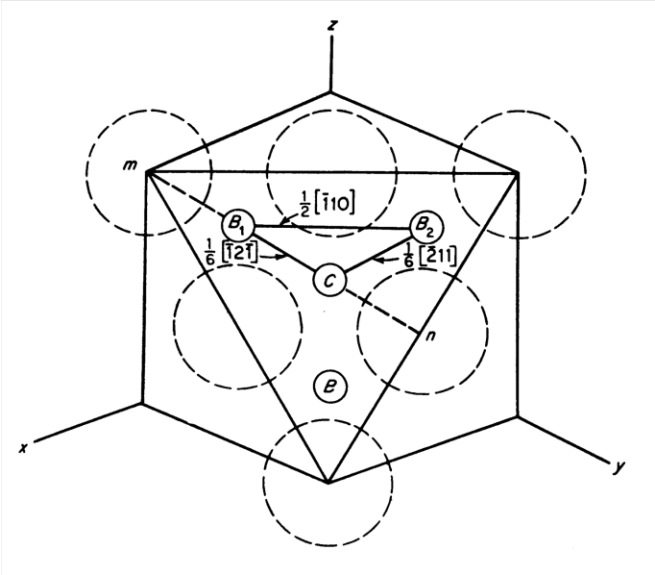

Figure 1.4: Orientation relationship of the partial dislocations $\frac{1}{6}[\bar{1}2\bar{1}]$, $\frac{1}{6}[\bar{2}11]$ to the primary edge dislocation on the (111) plane in an FCC lattice. The dotted circles represent the base *A*-layer of atoms, while the smaller circles represent the *B* and *C* layers as noted.[2]

Due to the equal lattice strains produced by each Shockley partial dislocation, each partial repels the other, thus creating an *extended dislocation*, where a discontinuity of the stacking order occurs. This extended discontinuity is referred to as a stacking fault, where the size of the stacking fault is determined by the balance of the additional surface energy created by the fault and the repulsive forces of the partial dislocations. During slip, the entire stacking fault moves as one entire defect, following the partial dislocations [1].

[2] Republished with permission of Cengage Learning from Physical Metallurgy Principles, Reza Abbaschian, Robert E Reed-Hill, 1992; permission conveyed through Copyright Clearance Center, Inc. See Appendix F for documentation to republish this material.

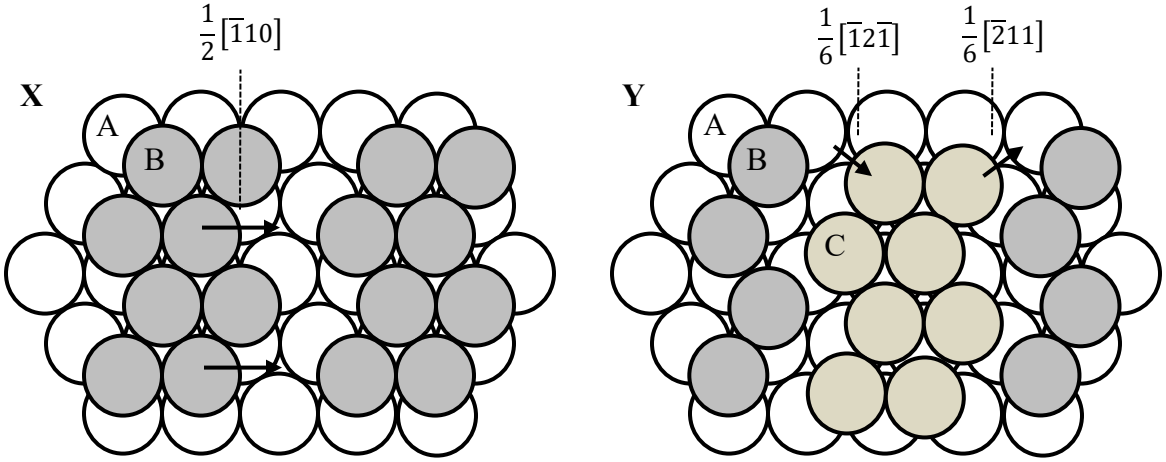

Figure 1.5: 2-dimensional projection of the (111) plane depicting two types of dislocation slip possible in the (111) plane, with the dislocations designated by arrows. **X)** Standard ½ $[\bar{1}10]$ edge dislocation motion in the *B* layer of atoms. The empty row of atoms represents the missing plane from the edge dislocation. **Y)** The partial dislocation sequence $\frac{1}{6}[\bar{1}2\bar{1}] + \frac{1}{6}[\bar{2}11]$, with the *C* layer atoms present in the extended dislocation.

1.2.2 Twin Faults in FCC Materials

As an alternative to slip during plastic deformation, twin deformation can also occur in face-centered cubic materials. Twin deformation typically occurs in materials with a limited amount of slip systems present (BCC/HCP) or at lower deformation temperatures and generally requires higher levels of stress than slip deformation in FCC materials [1]. In FCC materials, plastic deformation begins with slip and does not begin to twin until the material has been sufficiently work hardened to where the flow stress in the material has reached the stress required for twin deformation. During twin deformation, sections of the lattice are deformed to move to mirror positions across the defined twin boundary or twin plane, as shown in Figure 1.6. The crystallographic orientation of the lattice changes during twin deformation, as compared to slip deformation where the

crystallographic orientation stays the same. When compared to slip deformation, where single planes of atoms move, during twin deformation multiple planes of atoms move which involves large overall atomic movement, when compared to slip deformation on a single plane of atoms. Thus, the reason why twin deformation requires more energy than slip deformation.

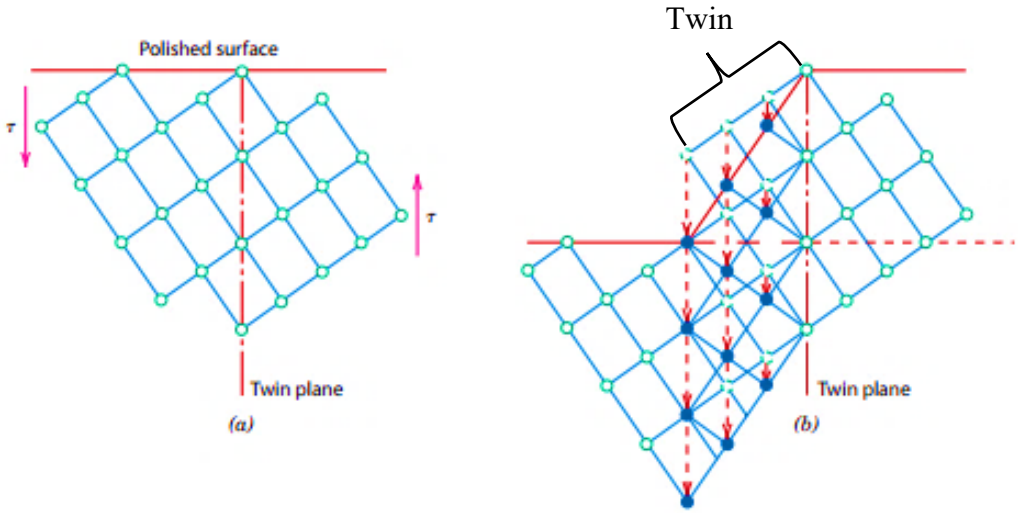

Figure 1.6: General diagram of twin deformation in a simple tetragonal lattice, showing the twin (mirror) planes and atomic movement in the twin fault. **A)** The un-deformed lattice, showing the future twin plane and applied stress. **B)** The twinned lattice after deformation, showing the twin fault and respective twin planes on either side of the fault. The theoretical lattice points from the just lattice rotation are shown (green circle) along with the deformed lattice points (blue circles) in the twin fault.[3]

In FCC materials, the stacking fault energy is directly related to the stress required to create a twin fault, since most of the energy required for twin deformation is a result of twin boundary creation and therefore the twin boundary surface energy. Therefore, twin

[3] Republished with permission of John Wiley and Sons from Fundamentals of Materials Science and Engineering: An Integrated Approach, 4th Edition, David G Rethwisch, William D. Callister, 2012; permission conveyed through Copyright Clearance Center, Inc. See Appendix F for documentation to republish this material.

deformation is more prevalent in lower stacking fault energy materials, such as brasses, copper alloys and high alloy austenitic steels. During twin deformation, the lattice can become oriented in a favorable position for slip to occur under the applied stress state, thus creating a favorable situation for slip deformation to occur next, rather than twin deformation [1]. The additional twin faults that are produced during deformation can act as additional barriers to dislocation motion, along with stacking faults produced during slip deformation. Previous work has shown that this effect can increase the strain hardening rate in copper alloys [13].

1.3 Austempered Ductile Iron

Austempered ductile iron, commonly referred to as ADI, is a relatively new material that was developed in the 1980/90s [7]. The primary difference between Austempered ductile iron and ductile iron is the heat-treatment process the material undergoes to reach the desired mechanical properties [14,15]. Immediately after austenitization, the material is quenched to a temperature above the M_s temperature and held for a set time to form an ausferrite microstructure that resembles a bainitic structure, with acicular ferrite and metastable austenite. The acicular ferrite nucleates along the prior austenite grain boundaries and grows within the individual grains around the graphite nodules. During the growth, the bulk carbon present is rejected into the remaining austenite, which stabilizes the austenite at room temperature. If the material is held too long at the austempering temperature, the carbon rich austenite begins to decompose to produce carbides (Fe_3C) and additional ferrite. The majority of the development in ADI has focused on optimizing the thermal processing steps to obtain various microstructures that

give desired mechanical properties. A few studies have shown that the thermally stabilized austenite undergoes a transformation to martensite under deformation, similar to austenitic stainless steels, which gives an increased strain-hardening response [16–18]. However, the understanding of the transformation is not as mature as the understanding in steels. The specific mechanisms of the transformation in ADI are not understood well and are assumed to be like the mechanisms in metastable austenitic steels, as outlined in Section 1.4. To the author's knowledge, no previous work has focused on characterizing the stacking faults directly in the austenite in ADI as a function of deformation. One study has characterized stacking faults in the austenite in ADI as a function of austempering time, showing that stacking faults are present at low austempering times, suggesting an annealing-out effect during longer austempering times [19].

1.4 304L Stainless Steel

Austenitic stainless steels (2xx, 3xx) are the most common types of stainless steel in use [12]. The additional nickel present stabilizes austenite over the ferrite present in ferritic stainless steel (4xx). Austenitic stainless steels can be classified in to two types, metastable and stable, where the stability refers to the strain hardening nature. The strain-hardening response is significantly increased when the austenite transforms to martensite upon deformation, due to the additional strain energy used in the transformation, rather than pure slip or twinning. Metastable austenitic stainless steels exhibit the increased strain-hardening response from the deformation induced transformation, where stable austenitic stainless steels have a reduced strain hardening response. The 301 and 304 types of stainless steel are typically considered metastable, where the 316 and 347 types

of stainless steels are considered stable. The L designation indicates a lower carbon content, where standard 304 stainless steel with about 0.02wt% C in 304L compared to 0.08wt% C in non-L 304. The martensite transformation in these types of austenitic stainless steels has been extensively studied and is well understood. The general sequence has been shown to include an intermediate ε (hexagonal-close packed) martensite phase which are nucleation sites for the BCC martensite, however it is hard to detect with x-ray diffraction. It is believed that this phase is formed from groups of stacking faults and is included in the Olson-Cohen model as a form of "shear-bands" that are used to describe the possible nucleation sites for the BCC martensite [20–25]. The 304L type of austenitic stainless steel was chosen based on previous literature results indicating that the deformation induced transformation occurs, thus providing a good baseline material to compare to the austempered ductile iron. The metallurgical reasoning behind the deformation induced transformation in the metastable austenitic stainless steels has been linked to the stacking fault energy. The stacking fault energy describes the elastic energy created in the lattice when a stacking fault is present and can also give information about the creep and dislocation cross-slip behavior. As the distance between the partial dislocations that create the stacking fault increases the cross-slip of these dislocations becomes more difficult [26,27]. It has been shown using Bayesian modeling of 75 historical experimental data sets that both Cr and C do not play a significant role in stacking fault energy, however Mn, Ni, N and Mo increase the stacking fault energy [27]. The increased Ni content in the 316 and 347 austenitic stainless steels therefore can explain the increased mechanical stability (resistance to martensite transformation) of the austenite, following the stacking fault energy increase with Ni content.

1.5 Measurement of Planar Fault Probabilities using X-ray Diffraction

After the introduction of x-ray diffraction to the suite of analytical tools of material scientists in the 1920's, studies on cold worked materials were conducted to understand the deformation structures of materials [28–32]. M.S. Paterson first introduced a theory on how to obtain stacking fault probabilities in crystalline materials in 1952, relating the probability of a fault being present to a distortion of the intensity in reciprocal space for hexagonal close-packed materials [33]. A diffraction phase shift due to the deviation from the normal stacking sequence expected in FCC materials causes this distortion in the reciprocal space intensity distribution. B.E. Warren expanded upon this analysis to include FCC, BCC and HCP materials along with extracting twin faulting probabilities in 1969 [34]. Warren assumed that,

1. The fault extends through the entire width (in the (111) plane) of the crystallites.
2. The fault densities are small (≤ 0.05) and uniform throughout all crystallites.
3. All the components of a reflection {hkl} have equal integrated intensities

The first assumption does not hold true when the average crystallite size, or coherent diffracting domain, is small enough to produce size broadening (>1000nm), as the powder pattern intensity equation is assumed to be integrated through an infinitely ($>>\lambda$) large crystallite which causes the intensity to be distributed very near the peak position. The second assumption holds true for most materials, however for heavily faulted materials this assumption becomes less accurate as the squared probability terms that are present in the full probability difference equations should be included. If any of the first two assumptions were not correct, then the third assumption becomes false as the various

components that make up a certain {hkl} will have differing integrated intensities. This third assumption also is not valid if texture is also present in the material, as that will also alter the integrated intensities. The theoretical basis for measuring stacking and twin fault probabilities in this work follows the procedure derived by Warren [34] and is described in brief here.

The derivation originates with the intensity given from a single unit cell crystal, which has been translated from the face-centered cubic cell a hexagonal unit cell to orient the crystal in such a way that the plane of interest for planar faulting (111) is in-line as a *00l* plane for simplification. The intensity from a single crystallite is then related to the displacement in a single layer that occurs from a different stacking sequence, which is caused by the atoms being in alternative locations in the individual *00l* (111) planes. The final reciprocal space intensity equation is given as Equation 1.2:

$$I = \psi^2 \sum_{m=-\infty}^{\infty} N_m \langle e^{i\phi_m} \rangle e^{\frac{2\pi i m h_3}{3}} \quad (1.2)$$

The ψ^2 term is equal to the summation of the intensity in the A_1A_2 directions, which is calculated immediately for simplification and isolation of the intensity to be a function of the average reciprocal space displacement term and diffraction vector. The full derivation of Equation 1.2 is given in Appendix A.

The diffraction vector from this reciprocal space intensity distribution is related to the probability of a planar fault being present in the structure using probability difference functions. These probability difference functions are derived from a probability tree of the *m*-2, *m*-1 and *m* layers which make up one unit-cell, where the *m*-2 layer must be

either in the *A*, *B*, *C* position of the standard *ABC* stacking sequence. The stacking fault (α) and twin fault (β) probabilities[4] are combined into single probability terms that give the probability that any *m*th plane is either the same (P_m^0) before (P_m^-) or ahead (P_m^+) of the starting layer in the standard stacking sequence (*ABCABCABC*). Taking the assumption that the crystallites in the sample are randomly oriented, that the faulting is distributed evenly across all crystallites then it can be assumed that both the P_m^+ and P_m^- are equal. This also mandates that for every crystallite with an *ABC* sequence, there will be a crystallite with the sequence, *CBA*, shifted 180° from the *ABC* sequence; therefore both P_m^+ and P_m^- are equal to $\frac{(1-P_m^0)}{2}$. Thus, the three probability terms may be combined into one single probability term, P_m^0. The singular probability term is combined with the reciprocal space shifts that are caused by the displacement of the atoms in a layer to calculate the average reciprocal space shift term, given by Equation 1.3.

$$\langle e^{i\phi m}\rangle = P_m^0 + (1 - P_m^0)\cos\frac{2\pi(h_1-h_2)}{3} \tag{1.3}$$

Where the P_m^0 is calculated from the difference functions to be Equation 1.4:

$$P_m^0 = \frac{1}{3}\left[1 + 2(-1)^m[1 - 1.5\alpha - \beta]^m\left(\cos m\left[\frac{\pi}{3} - \frac{\sqrt{3}\alpha}{2}\right] + \left(\frac{\beta}{s}\right)\sin m\left[\frac{\pi}{3} - \frac{\sqrt{3}\alpha}{2}\right]\right)\right] \tag{1.4}$$

This average reciprocal space shift term defines the criterion if an individual reflection that exists within a family of planes {hkl} is affected or unaffected by faulting, where an affected (a) plane is defined by $h_1 - h_2 = 3b \pm 1$ (P_m^0 is not canceled out) and an unaffected (u) plane is defined by $h_1 - h_2 = 3b$ (P_m^0 is canceled out). Following the first

[4] These probabilities, α & β, are not related to the α & β values used in the shear-band martensite nucleation model given in Equation 1.1.

assumption that the crystallites are large, the intensity will only be significant as the h_1 and h_2 terms approach the whole integer values of H_o and K_o which define the reflection in the hexagonal unit cell, therefore h_1 and h_2 can be replaced with H_o and K_o. This allows for the $h_1 - h_2$ term can be simplified to a single L_o, which is equal to $H_o - K_o$, giving the simplified criterion in the form of $L_o = 3b \pm 1$. The ± term is determined by the value of L_o (h+k+l), where either + or – is used to fulfill the criterion. For example, in the {111} family, a (-111) plane exists which gives an L_o value of 2, therefore for the (-111) plane, the ± value is + to make the entire value a multiple of 3 (2+1).

This criterion is used to define the reciprocal space intensity distribution that includes the affected and unaffected peaks, giving the total intensity from a single {hkl} family in reciprocal space, which is given in the final form of Equation 1.4.

$$I = \psi^2 \sum_m N_m[1 - 1.5\alpha - \beta]^{|m|} \left[\cos 2\pi m \left(\frac{h_3 - L_o}{3} - (\pm)\frac{\sqrt{3}\alpha}{4\pi}\right) \pm \frac{\beta}{\sqrt{3}} \sin 2\pi |m| \left(\frac{h_3 - L_o}{3} - (\pm)\frac{\sqrt{3}\alpha}{4\pi}\right)\right] \quad (1.5)$$

This is equivalent to the Fourier transform of the electron density, while accounting for possible broadening and/or shifting from stacking faults. The full derivation of Equation 1.5 is given in Appendix B.

In order to utilize this analysis on real-space (2θ) diffraction patterns, the reciprocal space intensity distribution is translated into real space through integration over all crystallites, following the powder pattern theorem derived by Warren [34]. Using the real-space power distribution, the shift and/or broadening in the pattern reflections {hkl} can be related back to the stacking fault probability (α) or twin fault probability (β). The presence of stacking faults in the structure gives a direct shift in the reciprocal lattice

point, thus causing a peak shift in the real space power distribution. The presence of twin faulting produces peak asymmetries, which is caused by the reciprocal space intensity distribution spreading out in one direction, while still being centered around the original reciprocal lattice point.

The direct relation between stacking fault probability (α) and peak shift present in the (111) and (200) reflections are given as Equations 1.5 and 1.6:

$$\Delta 2\theta = \left[\frac{90\sqrt{3}\alpha \tan\theta^{o}_{111}}{\pi^2}\right](0.25) \tag{1.6}$$

$$\Delta 2\theta = \left[\frac{90\sqrt{3}\alpha \tan\theta^{o}_{200}}{\pi^2}\right](-0.5) \tag{1.7}$$

Where the $\tan\theta^{o}_{hkl}$ term refers to the peak position of an un-faulted material, corresponding to the original reciprocal lattice position. These two equations can be combined to calculate the stacking fault probability from the shift in the peak difference between the two reflections as Equation 1.7. The full derivation of these equations starting from with the real-space power distribution derivation is given in Appendix C.

$$\Delta(2\theta_{200} - 2\theta_{111})^{\circ} = \frac{-90\sqrt{3}\alpha}{\pi^2}\left[\frac{\tan\theta^{o}_{200}}{2} + \frac{\tan\theta^{o}_{111}}{4}\right] \tag{1.8}$$

The twin fault probability can be related to the peak asymmetry, following a method developed by Cohen and Wagner that utilizes the same real-space power distribution function derived by Warren, which is described in Appendix D. The equations to calculate the twin fault probability for the (111) and (200) reflections are listed as Equations 1.9 and 1.10:

$$\Delta CG_{111} = 11\beta \tan\theta^{o}_{111} \tag{1.9}$$

$$\Delta CG_{200} = 14.6\beta \tan\theta^{o}_{200} \tag{1.10}$$

Where the $\tan\theta^{o}_{hkl}$ term refers to the peak position of the un-faulted material, like Equations 1.6-1.8, and the ΔCG_{hkl} term refers to the centroid shift from peak maxima (un-faulted material) for a specific reflection. Combining Equations 1.9 and 1.10, gives the twin faulting probability as a function of both the (111) and (200) reflection centroid shifts as:

$$\beta = \frac{\Delta\left(2\theta^{CG}_{111} - 2\theta^{max}_{111}\right) - \Delta\left(2\theta^{CG}_{200} - 2\theta^{max}_{200}\right)}{\left(11\tan\theta^{0}_{111} + 14.6\tan\theta^{0}_{200}\right)} \quad (1.11)$$

Equations 1.6-1.8 and 1.11 are the core equations that are used in this work.

2 Motivation/Hypothesis

Most of the previous work regarding the effect of deformation in the austenite to martensite transformation in austempered ductile iron has focused on the analysis of phase volume fraction as a function of deformation. The goal of this research was to evaluate the feasibility of measuring stacking or twin faults in ADI and the model system 304L stainless steel, to allow for further understanding of the deformation mechanisms prior to the martensite transformation. The 304L stainless steel was chosen as a baseline material to help give context to the ADI experiments, which was chosen based on previous literature as an ideal material for this analysis. A better understanding of faulting behavior in ADI could help further understand the kinetic models of this deformation induced transformation (austenite to martensite) present in ADI. Better understanding of this transformation could lead to tailored microstructures to give a higher strain hardening response for improved mechanical properties after deformation processing, or better material optimization for current applications.

2.1 1st Hypothesis

If the material containing metastable austenite (either 304L or ADI) is deformed in uniaxial compression or by filing, then the austenite (111) and (200) peaks on the diffraction will exhibit increased broadening and slight peak shifts because the stacking fault density increases before the martensite transformation occurs. Figure 2.1 illustrates the expected peak shift direction for the (111) and (200) peaks.

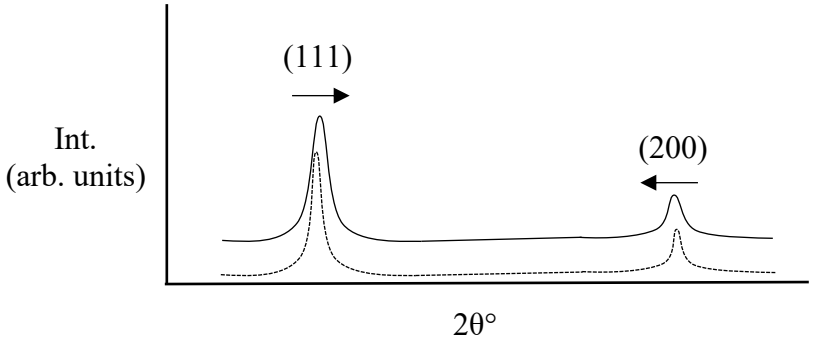

Figure 2.1: Simulated diffraction pattern of an austenitic (FCC) material, showing the expected peak shifts for the (111) and (200) peaks. The dotted line represented an un-faulted material, where the solid line represents a faulted material. The peaks are labeled, along with an arrow indicating the shift direction.

2.2 2nd Hypothesis

If the material containing metastable austenite (either 304L or ADI) is deformed in uniaxial compression or by filing, then the austenite (111) and (200) peaks on the diffraction will exhibit increased broadening and centroid shifts from peak maxims because the twin fault density increases from the applied deformation. Figure 2.2 illustrates the expected peak shift direction for the (111) and (200) peaks.

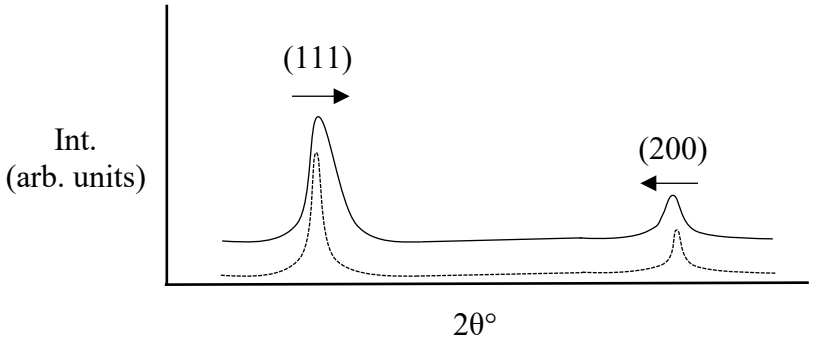

Figure 2.2: Simulated diffraction pattern of an austenitic (FCC) material, showing the expected centroid shifts for the (111) and (200) peaks. The dotted line represented a twin-free material, where the solid line represents a twinned material. The peaks are labeled, along with an arrow indicating the shift direction.

3 Experimental Methods

3.1 Sample Preparation

3.1.1 Austempered Ductile Iron

For the ADI samples, a commercially produced ductile iron (Dura-Bar Woodstock, IL) was utilized for metallurgical consistency. The material composition is given in Table 3.1.

Table 3.1: Nominal chemical composition for commercially produced ductile iron used as a base material in this experiment (wt%). The carbon equivalent of the material is 4.42, calculated via wt%C+0.33*wt%Si.

Fe	C	Si	Mn	Cr	Sn	Cu	Ni	V	Al	Ti	Mo
Bal	3.59	2.51	0.24	0.05	0.04	0.04	0.020	0.020	0.013	0.010	0.010

One heat-treatment cycle (two total steps) was used in this experiment; an austenitization step of 1 hour at 896°C and an austempering step of 1 hour at 382°C, with a final water quench after the austempering step. The samples were placed on a bed of graphite chips during the austenitization step to minimize decarburization. This heat treatment process was chosen based on previous literature results to achieve a high austenite volume fraction [14] and is similar an ASTM Grade 1 heat-treat process [35]. The samples were machined initially to a solid 40x80x10mm bar for heat-treatment. The heat-treatment was completed at Michigan Tech utilizing a standard box furnace and salt bath furnace with a salt composition of 50vol% KNO_3 and 50vol% $NaNO_2$. To maintain the proper mass ratio of material to salt in the salt bath (1:20), one bar was heat-treated at a time. After the austenitization in the box furnace in air was completed, the bars were transferred manually to the salt pot with an approximate 10 second time transfer time. Each bar was

swirled in the salt bath for 30 seconds during the initial immersion to help ensure proper quench time from the austenitization temperature. After heat-treatment the bars were machined to a final 10 mm diameter bar that was cut into 20 mm tall compression samples with the recommended 2:1 height to diameter ratio. All machining was done with cutting fluid to minimize sample heating and therefore microstructural changes. Five total samples were fabricated, one as an annealed control sample (A), with the additional four for compression testing with progressively larger amounts of plastic deformation (7, 10, 15 and 20%). A separate piece of heat-treated material was used for optical metallography.

3.1.2 304L Stainless Steel

A 304L stainless steel cold-rolled bar (Speedy Metals Appleton, WI) was used for compression sample preparation. The approximate composition of the material is listed in Table 3.2.

Table 3.2: Approximate chemical composition for commercially produced 304L stainless steel used as a standard material in this experiment (wt%). The material conforms to ASTM A276.

Fe	Cr	Ni	Mn	Si	P	S	C
Bal	18-20	8-12	2	1	0.045	0.030	0.030

The as-received rod was first annealed in a high-temperature box furnace at 1037°C for 30 minutes followed by a furnace cool to mitigate residual rolling texture present from the production process. The 12.7 mm diameter rod was cut into 25.4 mm sections to produce 2:1 length to diameter ratio compression samples. For compression testing, three separate samples (304L_A, 304L_B, 304L_C) were created from the annealed stock rod.

The target compression levels were 10%, 20% and 30% respectively. Filings were made with a hand smooth file (approx. 60 teeth per inch) from the annealed bulk rod to produce approximately 15 grams of approximately 100 mesh filings for x-ray diffraction analysis. An annealed sample was produced by vacuum encapsulated the filings with alumina batting as a plug to prevent filings being sucked into the vacuum pump. This quartz tube was sealed and then annealed at 1037°C for 15 minutes in a high-temperature box furnace followed by furnace cooling.

3.2 Compression Testing & Optical Microscopy

For compression testing, standard 150kN platens in an Instron 4206 load frame at a strain rate of 10^{-3} s^{-1} were utilized for testing. The strain was estimated using the crosshead measurements on the load frame used however the final strain was calculated using before and after measurements of the dimensions of the compression samples. Lubrication was used on each compression sample and little to no barreling was observed in each sample. After the compression was completed each ADI sample was cut perpendicular to the loading direction to obtain a representative surface for x-ray diffraction, as depicted in Figure 3.1. The second piece obtained was utilized for optical metallography. The 304L stainless steel compression samples were not cut to obtain a new x-ray diffraction surface, rather the top of each sample was used for both x-ray diffraction and optical metallography. Each sample was polished to a mirror finish prior to a final etch for structure observation; where the final step for the ADI samples was a 0.05μm alumina polish and for the 304L samples the final step was a 0.04μm silica polish. For ADI, a 3% Nital etchant was used to observe the overall structure, while

Klemm's I reagent (250mL sodium thiosulfate saturated solution & 5 grams potassium metabisulfite) was also used to tint the ferrite and better observe the retained austenite. For the ADI samples, the nodularity and nodule count were determined using a particle analysis routine in ImageJ.

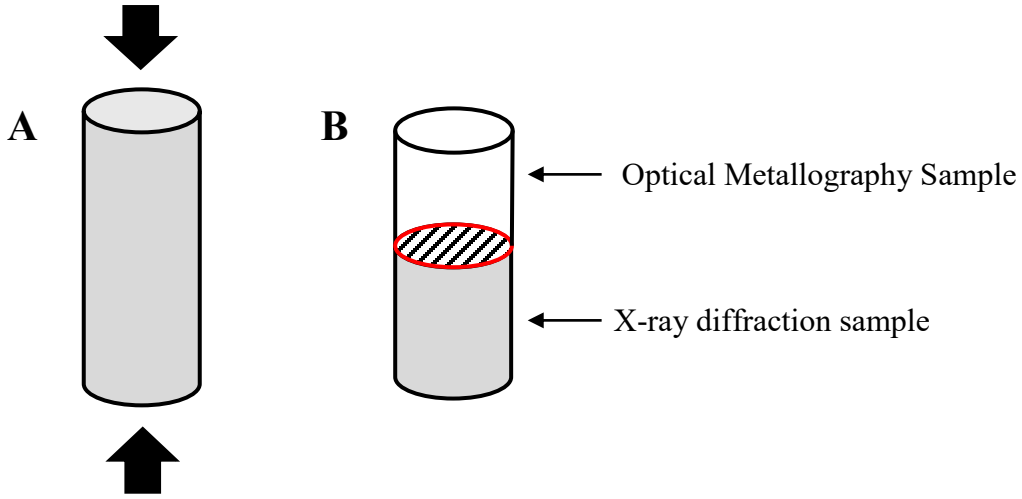

Figure 3.1: A) Diagram showing the orientation of the compression sample, with the arrows indicating the compression force direction**. B)** Diagram of the sample separation after cutting the compressed sample perpendicular to the compression direction showing the process for the ADI samples. The shaded section represents the x-ray diffraction sample, while the un-shaded section is the optical metallography sample section. The hatched area is the diffraction and optical metallography surface on each sample.

For the 304L stainless steel, an electrolytic etch consisting of 10% oxalic acid in a glass beaker at 6VDC for 60 seconds was used to observe grain boundaries. The list of all samples is given in Table 3.3.

Table 3.3: List of all samples used in the present work. The austenitization/austempering step refers to the entire heat treatment step and lists the temperature and time used. The theoretical sample deformation is listed for all samples except for the 304L filing.

	Austenitization Step	Austempering Step	Target Deformation (%)
ADI_A	896°C 120 minutes	382°C 60 minutes	0
ADI_B			7
ADI_C			10
ADI_D			15
ADI_E			20
304L_A	1037°C 30 minutes	None	10
304L_B			20
304L_C			30
304L Filings	1037°C 15 minutes		Unknown

3.3 X-ray Diffraction

Prior to collecting data, each sample for X-ray diffraction was polished following the same steps as the optical metallography samples (0.05μm alumina for ADI, 0.04μm silica for 304L), however the final polish step was followed by the same etch step and this combination was repeated three times (polish-etch, polish-etch, polish-etch) to remove any deformed layer created during the initial polishing process. X-ray diffraction data was collected on all the samples with a Scintag θ/θ diffractometer available at Michigan Tech. The tube power was set at 45kV and 35mA with a line focus configuration. The beam path optics included 1mm divergence and 2mm scatter slit on the incident beam and 0.5mm scatter and 0.3mm receiving slit on the diffracted beam. Both the incident and diffracted beam paths had Soller slits with a length of 25mm and 0.75mm spacing. The scan parameters varied for each set of samples to achieve good counting statistics and peak descriptions. The count time and step size parameters are listed in Table 3.4 for each sample type, while the scan ranges are listed in Table 3.5.

Table 3.4: Count time and step size parameters used in the X-ray diffraction experiments performed at Michigan Tech on each type of sample.

	Count Time	Step Size (2θ°)
ADI	20	0.02
304L Solid	20	0.02
304L Filings	20	0.01

Table 3.5: 2θ° Scan ranges used in the X-ray diffraction scans for each sample type. The specific peaks measured in each range are listed in the first row.

Sample Type	(111)γ, (110/101)α'	(200)γ (200/002)α'	(220)γ	(211/112)α'	(311)γ	(222)γ (220)α	(400)γ
ADI	41°-52°	63.5°-67.5°	72°-75°	81°-84°	87°-91.5°	97°-102°	
304L	41°-54°	63.0°-66.0°	73°-76°	79°-83°	87°-93°	94°-98°	115°-120°

The step size was chosen to have ≥10 points above the FWHM to describe the top of the peak well for peak position determination from profile fitting. The total scan range was made wide enough that each peak had tails that extended four times the FWHM on each side of the peak position to properly describe the tails to reduce the profile fitting errors. To fully understand the statistical variance of each sample, five individual scans were run over the austenite (111) and if present ferrite (110) peaks to obtain a 95% confidence interval of the peak positions. This error was assumed to be the maximum gross error as it included all sample errors and possible mounting errors. For each scan, the sample was remounted, and data collected following the same procedure each time. This individual peak error was used for both the (111) and (200) peaks in calculating the errors in stacking fault probability following the single peak method. An additional stainless steel 316L sample was measured over the (111) to (200) peak range (38.5 – 55.5° 2θ) to assess the error in the stacking fault probability (Eq. 1.8) with an error of the delta peak shift

($\Delta[2\theta_{200}\text{-}2\theta_{111}]$) calculated from replicate measurements of the total delta between the (200) and (111) peak positions. These additional measurements took place at the University of Virginia with a Panalytical Empyrean θ/θ diffractometer equipped with Cu radiation. The instrument was run at 45kV and 40mA with a 1mm divergence slit, 2mm scatter slit and 0.02rad Soller slit in the Bragg-BrentanoHD^{TM} optics module on the incident beam path. The diffracted beam path consisted of a wide scatter slit, 0.02rad Soller slit and a GaliPIX^{3D} area detector. No soller slits were utilized, however the optics configuration was configured to be as similar to the Scintag instrument as possible.

In addition to the data collected at Michigan Tech, a representative piece of each ADI sample was sent to the Advanced Photon Source (APS) at Argonne National Laboratory (ANL). Jonathon Almer at ANL kindly performed the experiment through a sample mail-in program available for the 1-ID beamline. Respective portions of the samples were attached to a sample "wheel" which can directly attach to the goniometer on the beamline for rapid analysis. The experiment was performed with x-rays at an energy of 71.67 keV from the APS Superconducting undulator through a high-energy monochromator with a bandpass[5] dE/E of 10^{-3}. The incident beam spot size was 0.01 mm^2 and data was collected on a Dexela 2923 area detector placed approximately 900 mm behind the samples. Instrumental correction was performed using an available NIST SRM cerium oxide powder placed in the sample wheel. The exposure time for the samples was approximately 1 second, which gave sufficient intensity given the overall brilliance of the

[5] The bandpass refers to the width (dE or dλ) of radiation (E or λ) the monochromator can remove, where the width needs to be less than the difference between the Kα1 and Kα2 energies or wavelengths.

source. The peak position errors for the diffraction data obtained from APS was calculated from the Pseudo-Voight profile fitting routine in Matlab© (Mathworks Natick, MA) performed at APS, which was assumed to be equivalent to calculating errors from replicate measurements based on previous data analysis performed by APS.

3.4 Diffraction Spectra Analysis

Rigorous data analysis was performed on the diffraction data obtained to achieve the best peak positions and profile fits possible. The raw data was first corrected for two functions that vary as a function of 2θ; atomic scattering factor, Lorentz-polarization factor. Then a cubic spline background fit was done to remove background noise from the samples, and a Rachinger correction was applied to remove the Cu $K_{\alpha 2}$ spectra from the pattern. From this point, two different programs were used to analyze the adjusted patterns: DMS-NT© (Scintag Inc. Cupertino, CA) for peak position, FWHM, profile shape and OriginPro© (OriginLab Northampton, MA) for centroid calculations. For the peak position (maxima) determination, the peaks were fit using a PearsonVII function and the resultant data was exported for easy addition to Excel. The PearsonVII function is described in Equation 3.1, and is similar to a Lorentz function raised to a power *m*. The *w* value is related to the peak width.

$$I(2\theta) = I_{Max}\left[\frac{w^{2m}}{\left(w^2+(2^{1/m}-1)(2\theta-2\theta_o)^2\right)^m}\right] \quad (3.1)$$

OriginPro also gave PearsonVII peak fit results and these results agreed with the results from DMS-NT, however only the centroid results from OriginPro were analyzed further. Peak positions, centroids and associated errors were utilized in the peak shift and centroid

analyses described earlier in Section 1.5 for the (111) and (200) peak positions. The error (200)-(111) delta for the 316L samples. was calculated following the same methods. These peaks were chosen because they had the lowest peak position errors due to their relatively high intensity and low broadening. The integrated intensities for the two majority phases, austenite and ferrite, were used to calculate relative phase fractions using the direct comparison method in a custom program VOLFRACT. The martensite peaks were not directly observed from the pattern, due to their inherent low scattering, therefore the martensite volume fraction was extracted assuming the ferrite volume fraction was for each sample.

4 Results

4.1 Austempered Ductile Iron

The standard ductile iron metrics of nodule count and nodularity were above the recommended requirements (nodule count >100mm^{-2} and 80% nodularity by area) that define suitable material for austempering. The nodule count and nodularity by area are given in Table 4.1 below.

Table 4.1: Nodule count and nodularity by area results listed for each austempered ductile iron sample. Each sample had the same heat-treatment cycle. The standard errors (95% confidence) are listed for each value.

Sample	Nodule count (mm^{-2})	Nodularity by area (%)
ADI_A	105 ± 9	91 ± 2
ADI_B	116 ± 12	93 ± 1
ADI_C	142 ± 23	82 ± 1
ADI_D	109 ± 4	94 ± 5
ADI_E	111 ± 6	85 ± 0 (34)

The actual levels of deformation obtained are listed in Table 4.2. The volume fraction of martensite vs deformation in general followed the expected trend, that with increasing l deformation the martensite volume fraction increased. As shown in Table 4.2, only sample D did not follow the expected trend, containing only 3% martensite.

Table 4.2: Volume fractions of austenite, ferrite and martensite calculated for each ADI sample. The volume fraction of graphite nodules was ignored for this analysis, due to the inability to observe representative diffraction peaks.

Sample	% Deformation	% Austenite	% Ferrite	% Martensite
ADI_A	0	42	58	0
ADI_B	5.3	39		3
ADI_C	9.3	34		8
ADI_D	14. (21)	39		3
ADI_E	21. (53)	30		12

The error in a single peak position was determined with replicate measurements to be approximately 0.005° 2θ for the annealed samples and 0.01° 2θ for the deformed samples, where 0.005° 2θ is also the smallest resolvable increment of the goniometer on the Scintag instrument. For the double peak difference shift analysis, the errors calculated from individual peak position errors were greater than or equal to the single peak analysis error values. For the stacking fault probabilities calculated from the APS data, the errors were on average an order of magnitude less than the errors from the Michigan Tech data. The calculated stacking fault probabilities and respective 95% confidence errors from the APS data are listed in Table 4.3.

Table 4.3: Stacking fault probabilities calculated from the data collected at the Advanced Photon Source at APL beamline 1-ID. The 95% error level is listed to highlight the significance of error propagation in this analysis. The angle listed indicates the peak shift source used in the calculation. The negative values are not expected and indicate that the shifts cannot be explained by stacking faults alone.

	α		
	$\Delta 2\theta_{111}$	**$\Delta 2\theta_{200}$**	**$\Delta(2\theta_{200}-2\theta_{111})$**
ADI_B	0.0009 ± 0.0002	-0.00361 ± 0.00007	-0.0060 ± 0.0002
ADI_C	0.0008 ± 0.0002	-0.00705 ± 0.00007	-0.0162 ± 0.0002
ADI_D	0.0014 ± 0.0002	-0.00618 ± 0.00007	-0.0105 ± 0.0002
ADI_E	0.0033 ± 0.0002	-0.00997 ± 0.00007	-0.0122 ± 0.0002

For the stacking fault peak shift analysis, the errors for the probabilities calculated from data collected at Michigan Tech were near or above 50% of the calculated result; reducing or eliminating the significance of the calculated stacking fault probabilities, as listed in Table 4.4.

While the twin fault probabilities were calculated from the Michigan Tech data, they were not calculated from the APS data due to the insufficient peak shape data required for centroid calculation. The austenite (111) peak was saturated due to over-exposure which unfortunately was not fixable with the beamtime allotted, thus the top part of the peak was unavailable for fitting and centroid calculation. The twin fault probabilities calculated from the Michigan Tech data are listed in Table 4.4. The errors associated with the stacking fault probabilities are significantly less than those associated with the probabilities calculated from the Michigan Tech data.

4.2 304L Stainless Steel

Optical metallographic analysis from the top surface of the compression samples showed, as expected, equiaxed grains with a relative grain size of 75μm. Compared to the target compression levels of 15, 20 and 25%, the actual compression levels attained in the samples were 8.27% for 304L_A, 20.26% for 304L_B and 21.78% for 304L_C. During compression testing, the platens reached their load limit at any strains higher than 22%. The volume fraction analysis was calculated for each level of deformation in the compression samples, however the martensite volume fraction did not go above 5%, which is slightly above the accepted detection limit of 2 volume % for any phase. For the filings, the volume fraction analysis was successful, and the filings were calculated to have approximately 45% martensite. The level of deformation in the filings could be estimated to be near the max elongation of 304L stainless (approx. 40% at 2" gage length), however it is impossible to measure the exact level of deformation. The stacking fault probabilities and twin fault probabilities calculated for the compression samples are

listed in Table 4.4. The 95% confidence errors are seen to be of the same magnitude as the calculated result for some of the compression sample results, while the 95% confidence errors for the filing sample results are less than the calculated result, giving significance to the results. Again, similar to the ADI samples, the double peak difference shift results had similar errors (from single peak position errors) to the single peak methods. The stacking and twin fault probabilities are inconsistent with the expected trends for the compression samples, where the 304L_C sample had a negative peak shift (wrong direction).

Table 4.5: Stacking and Twin faulting probabilities calculated for the ADI and 304L stainless steel samples from data collected at Michigan Tech. The 95% confidence errors are included to highlight the importance of error propagation in this analysis. The angle listed indicates the peak shift source used in the calculation. The errors in the twin fault probability and single peak were calculated from replicate measurements of the (111) peak.

	α			**β**
	$\Delta 2\theta_{111}$	$\Delta 2\theta_{200}$	$\Delta(2\theta_{200}\text{-}2\theta_{111})$	$\Delta(2\theta_{111}^{CG} - 2\theta_{200}^{CG})$
ADI_B	-0.001 ± 0.003	0.004 ± 0.002	0.007	0.0084 ± 0.005
ADI_C	-0.001 ± 0.003	0.004 ± 0.002	0.008	0.0086 ± 0.005
ADI_D	0.001 ± 0.003	-0.004 ± 0.002	-0.007	0.0158 ± 0.005
ADI_E	0.001 ± 0.003	-0.001 ± 0.002	0.002	0.0139 ± 0.005
304L_A	0.0002 ± 0.0002	0.0004 ± 0.0003	0.002	0.0031 ± 0.005
304L_B	0.0001 ± 0.0002	0.0015 ± 0.0003	0.005	0.0001 ± 0.005
304L_C	0.0009 ± 0.0002	-0.0033 ± 0.0003	-0.005	0.0023 ± 0.005
304L Filings	0.0019 ± 0.0006	0.0017 ± 0.0010	0.0141	-0.00005 ± 0.005

For the 316L sample, where double peak difference result had two possible error calculation options, from individual peak errors or from the double peak difference error, the double peak difference error gave much lower stacking fault probability errors,

indicating that the individual peak error method may overestimate the stacking fault probability error. These errors (double peak difference) were still on the order of the 316L sample stacking fault probability calculated from Equation 1.8. The comparison of these error methods is given in Table 4.5.

Table 4.5: Stacking fault probabilities and errors associated with the two possible methods of calculating the error in the double peak difference method; from single peak error terms and the double peak difference error term. These errors were calculated from five replicate measurements of the same sample.

	$\alpha - \Delta(2\theta_{200}-2\theta_{111})$		
	α	**Single Peak Error**	**Double Peak Error**
304L_A	0.002	± 0.004	-
304L_B	0.005	± 0.004	-
304L_C	-0.005	± 0.004	-
304L Filings	0.0141	± 0.0167	-
316L	0.0031	± 0.0141	± 0.0037

5 Discussion

5.1 Planar fault measurement via X-ray diffraction

The determination of planar faults, either stacking or twin, with x-ray diffraction can be difficult because of the very small peak shifts and/or centroid shifts that occur as a result of planar faults. Table 5.1 shows the theoretical peak shift values in the ADI samples for both stacking and twin faulting, along with an estimated distance between faults. The single peak shifts were calculated with Equations 1.6 and 1.7 by fixing a given stacking fault probability.

Table 5.1: Calculated stacking and twin fault peak shifts based on given faulting probability. The average distance between faults was calculated using an average (111) d-spacing of 0.209nm, which was the average for all the ADI samples. The peak shifts are calculated to the 5th decimal for perspective. The twin fault probabilities are based on centroid shifts.

$\alpha \mid \beta$	Spacing between faults (nm)	$\alpha - \Delta 2\theta_{111}$	$\alpha - \Delta 2\theta_{200}$	$\beta - \Delta 2\theta_{111}$	$\beta - \Delta 2\theta_{200}$
0.0001	2090	0.00016	-0.00037	0.00043	-0.00068
0.0005	418	0.00079	-0.00187	0.00217	-0.00341
0.001	209	0.00158	-0.00375	0.00434	-0.00682
0.005	41.8	0.00789	-0.01873	0.02172	-0.03412
0.01	20.9	0.01578	-0.03746	0.04344	-0.06825
0.05	4.18	0.07890	-0.18732	0.21719	-0.34125
0.1	2.09	0.15780	-0.37464	0.43438	-0.68249

As shown, until stacking fault probabilities are ≥0.001, then the peak shift or centroid shift is very small ($\leq 0.00158° \ \Delta 2\theta_{111}$, $\leq 0.00375° \ \Delta 2\theta_{200}$) and would require very careful experimental procedures and precise equipment to measure. This is further complicated by the error that is present in the experiment, from peak position determination. The results for all but a few samples have large error values, on the same magnitude as the

calculated result. Error propagation for the stacking fault (Equations 1.6 and 1.7) for single peak analysis yields the RMS sum of partial differentials given in Equation 5.1.

$$\delta\alpha[\text{single peak}] = \sqrt{\left(\left(\frac{\partial\alpha}{\partial\Delta 2\theta_{hkl}}\right) * (\delta\Delta 2\theta_{hkl})\right)^2 + \left(\left(\frac{\partial\alpha}{\partial\theta_{hkl}}\right) * (\delta\theta^o_{hkl})\right)^2} \quad (5.1)$$

It is clear from Equation 5.1 that both the errors in the $\Delta 2\theta$ shift and θ position, where the shift consists of the errors in both the annealed and deformed (faulted) peak positions and the θ^o_{hkl} consists of half the error in the annealed peak position. The error propagation for the double peak shift stacking fault probability analysis (Equation 1.8) yields the RMS sum of partial differentials given in Equation 5.2.

$$\sqrt{\left(\left(\frac{\partial\alpha}{\partial\Delta(2\theta_{200}-2\theta_{111})}\right) * (\delta(\Delta(2\theta_{200}-2\theta_{111}))\right)^2 + \left(\left(\frac{\partial\alpha}{\partial\theta_{200}}\right) * (\delta\theta_{200})\right)^2 + \left(\left(\frac{\partial\alpha}{\partial\theta_{111}}\right) * (\delta\theta_{111})\right)^2} \quad (5.2)$$

From Equation 5.2, the total error in the stacking fault probability calculation is due to the error in double peak shift term and the error in the θ_{111} and θ_{200} terms. The double peak shift error could be derived following two methods, as outlined in Section 3.4 and 4; by either utilizing each individual peak position error term (from replicate measurements of $2\theta_{111}$ & $2\theta_{200}$ for both the annealed and deformed samples) or by measuring the entire peak range including both the $2\theta_{111}$ & $2\theta_{200}$ peaks and calculating an error in the entire difference. As the results in Table 4.4 show, the error is much larger when individual peak errors are used, compared to the error from the difference between two peaks. The double peak error allows for a reduction in the overall experimental error by significantly reducing the experimental errors that are caused by the instrument that can vary from scan to scan, because both peak positions are measured on the same scan. Although instrumental errors are a function of 2θ, the peak positions of the (111) and (200) are so

close together that these instrumental errors should be approximately equal for each peak. This rationale indicates that for calculating a stacking fault probability, the error should be calculated from replicate measurements of entire $2\theta_{111}$ & $2\theta_{200}$ range to accurate determine the error in the probability. The individual peak error terms are calculated from the peak error from the annealed peak position, from which the individual peak positions are derived from in Equation 5.2. For the twin fault probability calculation, the error propagation yields:

$$\sqrt{\left(\partial\beta 1 * \delta\left(\Delta\left(2\theta_{111}^{CG} - 2\theta_{111}^{max}\right)\right)\right)^2 + \left(\partial\beta 2 * \delta\left(\Delta\left(2\theta_{200}^{CG} - 2\theta_{200}^{max}\right)\right)\right)^2 + \left(\frac{\partial\beta}{\partial\theta_{111}} * \delta\theta_{111}\right)^2 + \left(\frac{\partial\beta}{\partial\theta_{200}} * \delta\theta_{200}\right)^2} \quad (5.3)$$

Where the $\partial\beta 1$ and $\partial\beta 2$ partial differentials are abbreviations in place of partial differential taken with respect to the centroid shift in the (111) and (200) peaks respectively. Similar to the error propagation for the stacking fault probability equations, the single peak *maxima* positions, (111) & (200), for the annealed and the errors in the centroid shift from maxima for each peak are factors in the total error for the twin fault probability. The error propagation terms are detailed further in Appendix E.

Following the error propagation, attention must be paid to the experimental setup and sample preparation to minimize any errors that may occur during experimentation. There are a wide variety of effects that can cause changes in the diffraction pattern, mainly restricted to two groups; extrinsic (instrumental) or intrinsic (material defects) errors. The extrinsic (instrumental) errors include both sample displacement, beam misalignment and/or axial divergence. During the sample preparation, care was taken to ensure that sample displacement errors were kept to a minimum and were at the very least consistent

throughout every sample. The sample displacement errors are inversely proportional to the diffractometer radius and thus the largest diameter goniometer available should be used in this type of experiment. There was no apparent evidence for a misaligned beam and therefore errors from the beam misalignment are assumed to be minimal. The axial divergence was limited on this instrument due to the presence of Soller slits on both the diffracted and incident beam paths and the asymmetry caused by axial divergence was assumed to be minimal. This type of analysis produced smaller errors when compared to the single peak analyses that were performed, for both sample types.

The intrinsic errors from sample defects can include sample transparency (low linear-absorption) and sample fluorescence (sample K-edge near beam K-edge) along with structural defects such as stacking faults, twin faults, internal stresses, grain-boundaries, and chemical inhomogeneities. For the materials selected (ADI,304L and 316L steel) and the soft x-rays used (Cu-radiation) the linear-absorption coefficients are sufficiently high ($304.4 g/cm^3$) to eliminate possible transparency effects. Sample fluorescence from Fe-based materials is not an issue with the Michigan Tech instrument because of the presence of the graphite monochromator which eliminates all other wavelengths outside of CuKα. For the structural defects, a wide variety of diffraction pattern distortions can occur from the intrinsic defects. Isolating the stacking or twin faults as a cause of peak shift is difficult given the other possible causes, such as grain boundaries, sub-boundaries, internal stresses, coherency strains and chemical heterogeneities. [36] Both the stacking fault and twin fault probability analyses assume that the peak shift is solely

from stacking faults or twin faults respectively, however if the sample contains other sources for peak shifting this assumption cannot be made as confidently.

5.1.1 Difficulties with ADI Measurement

In the austempered ductile iron samples, the interpretation of the peak shift results became problematic with the use of one annealed sample as a baseline for each of the deformed samples. The experimental method was modified for the 304L stainless steel, where a measurement was made on each sample before and after the deformation, to eliminate the effects from chemical inhomogeneities that exist from sample to sample. The localized differences in alloy content, specifically manganese and tin are theorized to be a possible factor in the inconsistent peak shift results gathered from the ADI samples at Michigan Tech, where during the austempering heat-treatment the Mn and Sn wt% could vary across the bulk retained austenite present. Previous literature has shown that alloying elements can segregate during the initial production of ductile iron prior to austempering; where Mn and Mo segregate to the regions far from the graphite nodules and Ni and Si segregate to regions near the graphite nodules. [37] This effect on the inconsistent peak shift is believed to not be a large factor in the data measured at APS, due to large bulk sample measurement area achieved with the experimental setup (thru-sample measurement). If the carbon is uniform across the bulk austenite, assumed because of the relatively fast diffusion of carbon in austenite, the lattice parameter of the FCC austenite can be determined from the atomic radii of the atoms present on the primary lattice sites. Manganese has an atomic radius of 0.112nm which is smaller than iron (0.124nm) and would result in a smaller overall lattice parameter with increasing Mn

content. Tin has a larger atomic radius (0.158nm) than iron and would therefore cause a larger lattice parameter with increasing content. With a 0.24wt% change in manganese content in the austenite (double the amount present in bulk), the lattice parameter will change by -0.00004Å, which would only shift the (111) and (200) peaks by 0.00001° and 0.000012° 2θ, which isn't significant enough to influence the total shift for these levels of faulting. The change in wt% for Mn would have to be ≥ +5.00 wt% to achieve high enough shifting levels to affect this type of analysis, where a +5.00 wt% change would shift the (111) and (200) peaks by 0.000271° and 0.000322° 2θ. For tin, a change in wt% of ≥ +1.00 wt% would be required to achieve a significant shift; (111) by 0.00092° and (200) by 0.00110° 2θ). Localized changes in the M_s due to segregation should not be a significant issue, as empirical formulae developed for iron-carbon alloys [38] show that Mn does not significantly change the M_s temperature when compared to the effect of carbon. A positive 0.24wt% change in Mn will decrease the M_s temperature by approximately 7.9°C according to the Andrews formula [39], while still being well below room temperature at approximately -290.71°C.

An additional source of error that was discovered during experimentation was the effect of carbon wt% on the tetragonality of the martensite after the transformation. The martensite transformation is assumed to be diffusion-less, thus the martensite takes on the chemical composition of the parent austenite phase, which in the ADI sample was determined to be ~1.9wt%. Due to this increased carbon percentage compared to the 304L stainless steel (≤0.04wt%), the martensite is highly tetragonal. The carbon present in the octahedral sites in austenite lies directly on the c-axis in the martensite after the

transformation. The carbon present in the martensite will therefore influence the length of the c-axis, which determines the tetragonality of the unit cells. The (110), (200) and (211) peaks are split, giving the (101)/(110) (002)/(200) and (112)/(211) separate peaks. Table 5.3 shows the calculated martensite peak positions, along with the austenite peak positions in each of the ADI samples tested.

Table 5.2: Calculated theoretical peak positions in 2θ° for martensite, transformed from the parent austenite. The peak-splitting is due to the carbon present in the unit cell, which lies on the c-axis. The d-spacing was calculated using the $CuK\alpha_1$ wavelength and lattice parameter of the parent austenite for each sample.

Sample	**(101)**	**(110)**	**(002)**	**(200)**	**(112)**	**(211)**
B	43.22	45.07	59.83	65.65	77.95	81.89
C	43.16	45.09	59.60	65.68	77.76	81.87
D	43.18	45.09	59.68	65.67	77.83	81.88
E	43.22	45.07	59.85	65.64	77.96	81.89

At these high carbon levels, the (101) martensite reflection is very close to the (111) austenite reflection, within 0.2° 2θ and thus it would be difficult to deconvolve the austenite peak from the martensite peak for analysis, without exact knowledge of the martensite peak shape and intensity. Due to the low scattering factors and relatively low volume fractions of the martensite, the intensities for these peaks should be very low so an assumption can be made that it is not a significant effect on the (111) austenite peak, however it is unclear whether this is a valid assumption. Another assumption that was made during the experiment was that the uniaxial compression tests produced strains that were uniformly distributed between both the ferrite and austenite phases in the ADI samples. Previous studies have shown that the exact nature of the stress state in the

austenite can affect the martensite transformation in steels and this assumption was made for the sake of simplicity [40,41].

5.1.2 Peak Position Determination Errors

Additional errors can arise during the peak fitting procedures, to determine the exact peak positions and centroids necessary for both stacking and twin faulting density measurement. Traditional peak fitting routines rely on a weighted fit to the error from counting statistics, therefore both the step size (increase data points) and count time (minimize counting statistics error) are important to collect quality data an obtain accurate peak positions. Comparing the data collected at Michigan Tech to the data collected at APS, the errors are significantly reduced in the data at APS indicating that utilization of a synchrotron source can help eliminate experimental errors. The advantages to using a synchrotron source stem from the significant increase in source brilliance (71.67keV at APS, 8.0478keV for CuKα_1 at Michigan Tech), which allows for a bulk sample measurement via transmission at APS, compared to standard diffraction in the lab instrument at Michigan Tech. The beam collimation is also significantly increased, giving reduced beam divergence errors when compared to the lab diffractometer at Michigan Tech.

In addition, replicate measurements should be made in-order to quantify the other extrinsic errors in the experimentation. The errors given in Section 4 are a result of replicate measurements on respective samples and are assumed to be representative of the max errors. As discussed in Section 4.1, the error in the annealed samples for both ADI and 304L steel were concluded to be 0.005° 2θ, which is the same as the smallest

increment for the Scintag θ/θ diffractometer used in the experimentation. While this value seems small, considering the theoretical peak shifts calculated from Equations 1.6 and 1.7 (Table 5.1), once it is propagated with the errors in the deformed samples (0.01° 2θ) it becomes significant for the final probability calculation in the single peak shift analysis. For the double peak analysis, the error from the instrument is significantly reduced in the peak difference ((200)-(111)) because both peak positions are measured in the same scan. Overall, the error propagation indicates that very precise instrumentation and experimental parameters are required to measure the small faulting probabilities (≤0.005) that are present in these materials.

Alternative methods for obtaining fault probabilities, such as Fourier analysis are a feasible option for comparison to the peak shift values, as peak broadening is also a function of both stacking faults and twin faults and in a broader context microstrain and coherent diffracting domain size. The data collected at Michigan Tech did not produce intensities on the higher-order peaks, (222) and (400), that are required to perform these types of analyses and obtain coherent results. Utilization of a high-brilliance source like a synchrotron or rotating-anode diffractometers can allow for suitable intensities needed for Fourier analysis, especially for the ADI samples that at most contain approximately 40% austenite.

5.2 Interpreting Calculated Fault Probabilities

In general, any source of change to the lattice parameter and thus d-spacing on specific planes will cause peak shifts as defined by the Bragg equation ($\lambda=2d\sin\theta$). Therefore, the

results must be interpreted with a perspective on all other possible effects. For example, during the martensite transformation, one could postulate that new grain boundaries are being created in the process, thus the stacking fault probability result could be affected by additional peak shifting from grain-boundaries. Another theoretical source of peak shifting could be residual macro-stresses present in the material, which would shift all the peaks in a diffraction pattern. The peak shift direction will depend on the direction of the stress (tensile or compression) and vary as a function of cotθ (Equation 5.1), meaning higher angle peaks will exhibit more shift than lower angle peaks for a given stress.

$$\frac{\Delta a}{a} = -\cot\theta\Delta\theta \tag{5.1}$$

5.2.1 Stacking Fault Probabilities

Comparing the measured peak shift values in Tables 4.3 and 4.4 to the theoretical peak shift values in Table 5.1, it is apparent that there are some other factors influencing the peak shift in the ADI material. A peak shift caused by chemical homogeneities could best explain the negative probability values seen in the ADI samples. According to the theory outlined in Section 1.5 and in Warren [34], the peak shift direction depends on the plane; where (111) shifts to higher 2θ and (200) shifts to lower 2θ. Looking at the APS collected data for the ADI sample B, the $\Delta 2\theta_{111}$ is very small and the $\Delta 2\theta_{200}$ is a more negative than expected for the α level. This indicates that a possible uniform shift to smaller 2θ might exist.

This uniform directional shift could possibly be caused by a higher wt% of manganese in the compression sample, compared to the "annealed" sample used, which is possible

given the experimental procedure used for the ADI. Considering the processing history of the austempered ductile iron samples; commercially produced ductile iron along with an hour austenitization step, it is unlikely that the substantial amounts of segregation required to shift the peaks is present in the bulk samples. As discussed in Section 5.1.1, with the relatively small irradiated sample area measured in the Michigan Tech data this could be more influential in the data result. However, with the larger irradiated area measured in the APS data this reasoning becomes less likely. A chemical analysis using X-ray dispersive spectroscopy (small lateral resolution) and X-ray fluorescence (bulk) would help to determine whether these possible chemical heterogeneities are a significant factor in this type of analysis. In addition, each sample should be measured before and after the deformation is applied, in order to avoid inconsistencies that arise from using different sections of the same material for annealed and deformed (faulted) samples.

It is also possible that the additional coherency strains that are created during the martensite transformation are creating an additional peak shift in the austenite diffraction pattern. Previous literature has shown that the martensite transformation introduces internal long-range coherency strains [42], which have also been linked to increasing the austenite thermal stabilization [43,44]. These coherency strains are a product of the volume change that occurs when austenite transforms to martensite, following the relation given in Equation 5.2. [45]

$$V_{\gamma\rightarrow\alpha} = 4.64 - 0.53 * \mathrm{wt\%C} \quad (5.2)$$

Assuming a carbon wt% of 1.9%, the volumetric strain created during the transformation from austenite to martensite would be approximately 3.6%. With the known amount of

austenite transformed into martensite, the total volume change can be calculated for each ADI sample. The calculated total strain in the austenite resulting from the partial transformation to martensite is given in Table 5.3.

Table 5.3: Total volumetric strain, Δa and peak shift values calculated for each ADI sample. The change in lattice parameter (Δa) was calculated following Equation 5.1. The a_o used for the calculation was 3.63Å, which is the average measured lattice parameter for the ADI samples.

Sample	Martensite vol%	Transformation Strain (1.9 wt% C)	Total Strain	Δa (Å)	$\Delta 2\theta_{111}$	$\Delta 2\theta_{200}$
ADI_B	3%	3.63%	0.109%	0.004	-0.000881	-0.001046
ADI_C	8%		0.290%	0.011	-0.002422	-0.002875
ADI_D	3%		0.109%	0.004	-0.000881	-0.001046
ADI_E	12%		0.436%	0.016	-0.003523	-0.004182

With the calculated Δa for each sample, the peak shifts for the (111) and (200) peaks can be calculated, also following Equation 5.1. Comparing these peak shift values to the theoretical shifts listed in Table 5.1, these values are large enough to play a significant factor in the overall stacking fault calculation. An additional x-ray stress/strain analysis could be conducted to help decide whether these long-range coherency strains are present in the sample.

5.2.2 Twin Fault Probabilities

The twin-fault probabilities calculated from the ADI samples do show a high density of twin faults, especially at higher deformation levels. However, it is unclear whether the asymmetry is solely due to the presence of twin-faults from this data alone. Asymmetry from intrinsic (sample) sources indicates the intensity is skewed towards one end of the range of d-spacings (low-side or high-side asymmetry), that define a single family of

planes (reflection). As discussed in Section 1.2.2, twin faults in an FCC material produce the same structure, with an orientation change compared to the parent lattice. Following the general definition of asymmetry, it can be theorized that if twinning is assumed to be the dominant mechanism of deformation, then the asymmetry is defined by presence of the smaller or larger d-spacings present at the twin-boundaries. These additional spacings that are consistent through the boundary in effect skew the intensity distribution towards the low-angle or high-angle side of the theoretical Bragg peak. In addition to twin faults, peak asymmetry can be caused by a multitude of material defects, including dislocation pile-up at grain boundaries, coherency strains and chemical heterogeneities. Following real-space power distribution (Equation C.18) and the sin coefficient (Equation C.20) given in Appendix C, stacking faults can enhance the asymmetry caused by twin faulting alone, by increasing the $Z^{n/q}$ term. Taking this into account, the assumption that the asymmetry is solely from asymmetry is less clear if we assume that stacking faults are present as indicated by the results given in Tables 4.3 and 4.4. Additional studies, such as scanning transmission electron microscopy or field-emission electron microscopy might be able to help identify whether the austenite is twinned, or if the asymmetry is caused by other factors such as dislocation pile-up by visually observing the structure.

6 Conclusions

The measurement of planar fault densities is inherently complex, due to the nature of the diffraction condition where any change in the lattice structure causes deviations from the theoretical perfect distribution of intensity. Isolating individual perturbation sources, like planar faults, can be done but the results must be interpreted with the correct perspective on the entire material and experimental conditions. The feasibility of measuring the planar fault densities in austempered ductile irons is complicated by the following factors:

1. Limited volume fraction of austenite (FCC) phase present, which affects the overall intensity that can be measured. This can be accounted for by utilization of high-brilliance sources like synchrotron or rotating anode x-ray sources.
2. The loss of austenite due to the deformation-induced transformation that occurs after plastic deformation.
3. Isolation of all other defects that cause peak shifts that are common when deforming materials, like dislocation build-up, changing crystallite sizes and coherency strains that may change during the austenite to martensite transformation. Assumptions must be made in-order to interpret the data properly.

Additional studies to gain additional perspectives on the deformation behavior of ADI, such as transmission-electron microscopy could help corroborate the information interpreted from the diffraction data. It is feasible that the coherency strains introduced in the remaining austenite, because of the partial transformation to martensite, are affecting the measurement results, by shifting the entire diffraction patterns which alters the delta values used in the analysis for planar fault probabilities. The errors in the peak position determination were also significant, indicating that a more precise goniometer or alternative sample creation method should be utilized for better results. The errors in the

peak shifts were an order of magnitude less with the data acquired from the synchrotron beamline source at APS, however for both data sets the peak difference shift ($\Delta(2\theta_{200}-2\theta_{111})$) analysis method gave smaller errors. The smaller errors associated with the double peak difference shift are due to the significant reduction in the instrumental errors normally associated with the peak shift analysis because both peak positions are measured on the same scan, therefore they apply to each position nearly equally. These will vary slightly between each peak position because of the dependence of the errors on 2θ, however the $2\theta_{111}$ and $2\theta_{200}$ positions are close enough that these errors do not vary significantly. Any attempt to measure stacking fault probabilities should utilize this method (double peak difference) to obtain the most precise results.

With proper measurement parameters, Fourier analysis should be performed to complement planar fault densities measured from peak and centroid shifts, as the broadening can give information about microstrain and coherent diffracting domain size in addition to information about the planar faulting. Both can be useful in determining if the assumptions (no texture, no size broadening) made for the peak shift and centroid shift values were correct. In addition, visually measuring stacking faults or twin faults in the austenite and understanding the exact orientation relationship between the austenite and martensite could help better understand the planar fault probabilities measured with the technique used in this work.

Further development of these methods could give more clues about the specific transformation behavior in austempered ductile irons. The transformation does occur in these materials according to these results, however it is not clear whether stacking faults

play a clear role in the transformation from these results alone. Stacking faults can be measured in ADI if the considerations discussed are considered in the experimental design and careful experimentation is performed.

7 References

[1] R. Abbaschian, R.E. Reed-Hill, Physical Metallurgy Principles, Cengage Learning, 2008.

[2] K. Bhattacharya, Microstructure of Martensite: Why it Forms and how it Gives Rise to the Shape-memory Effect, OUP Oxford, 2003.

[3] I. Tamura, Deformation-induced martensitic transformation and transformation-induced plasticity in steels, Met. Sci. 16 (1982) 245–253.

[4] C.M. Tamarelli, AHSS 101 The Evolving Advanced High-Strength Steels for Automotive Applications, Steel Mark. Dev. Inst. Rep. Southf. MI USA. (2011).

[5] S. Mendelson, The Kurdjumov-Sachs, Bogers-Burgers, Nishiyama, and Zener models for martensite formation in FCC→ BCC, Scr. Metall. 11 (1977) 375–382.

[6] G.B. Olson, M. Cohen, A general mechanism of martensitic nucleation: Part I. General concepts and the FCC → HCP transformation, Metall. Trans. A. 7 (1976) 1897–1904. doi:10.1007/BF02659822.

[7] G.B. Olson, M. Cohen, A general mechanism of martensitic nucleation: Part II. FCC → BCC and other martensitic transformations, Metall. Trans. A. 7 (1976) 1905–1914. doi:10.1007/BF02659823.

[8] G.B. Olson, M. Cohen, A general mechanism of martensitic nucleation: Part III. Kinetics of martensitic nucleation, Metall. Trans. A. 7 (1976) 1915–1923. doi:10.1007/BF02659824.

[9] A.J. Bogers, W.G. Burgers, Partial dislocations on the {110} planes in the B.C.C. lattice and the transition of the F.C.C. into the B.C.C. lattice, Acta Metall. 12 (1964) 255–261. doi:10.1016/0001-6160(64)90194-4.

[10] G.B. Olson, M. Cohen, Kinetics of strain-induced martensitic nucleation, Metall. Mater. Trans. A. 6 (1975) 791–795.

[11] J. Rösler, H. Harders, M. Baeker, Mechanical behaviour of engineering materials: metals, ceramics, polymers, and composites, Springer Science & Business Media, 2007.

[12] F.C. Campbell, ed., Elements of metallurgy and engineering alloys, ASM International, Materials Park, Ohio, 2008.

[13] L. Remy, Kinetics of fcc deformation twinning and its relationship to stress-strain behaviour, Acta Metall. 26 (1978) 443–451.

[14] T.N. Rouns, K.B. Rundman, Constitution of Austempered Ductile Iron and Kinetics of Austempering.(Retroactive Coverage), Trans. Am. Foundrymens Soc. 95 (1987) 851–874.

[15] T.N. Rouns, K.B. Rundman, D.M. Moore, On the Structure and Properties of Austempered Ductile Cast Iron.(Retroactive Coverage), Trans. Am. Foundrymens Soc. 92 (1984) 815–840.

[16] S. Daber, P.P. Rao, Formation of strain-induced martensite in austempered ductile iron, J. Mater. Sci. 43 (2008) 357–367.

[17] J.L. Garin, R.L. Mannheim, Strain-induced martensite in ADI alloys, J. Mater. Process. Technol. 143–144 (2003) 347–351. doi:10.1016/S0924-0136(03)00452-7.

[18] D. Guzmán, L. Navea, J. Garín, C. Aguilar, A. Guzmán, Estudio de la influencia del Cu y Ni en la cinética de transformación martensítica inducida por deformación en fundiciones nodulares austemperadas, Rev. Metal. 49 (2013) 213–222.

[19] J.D. Hermida, Stacking faults in austempered ductile iron, Scr. Mater. 34 (1996) 1735–1739.

[20] A. Das, P.C. Chakraborti, S. Tarafder, H. Bhadeshia, Analysis of deformation induced martensitic transformation in stainless steels, Mater. Sci. Technol. 27 (2011) 366–370.

[21] J. Dash, H.M. Otte, The martensite transformation in stainless steel, Acta Metall. 11 (1963) 1169–1178.

[22] A.K. De, D.C. Murdock, M.C. Mataya, J.G. Speer, D.K. Matlock, Quantitative measurement of deformation-induced martensite in 304 stainless steel by X-ray diffraction, Scr. Mater. 50 (2004) 1445–1449.

[23] S.S. Hecker, M.G. Stout, K.P. Staudhammer, J.L. Smith, Effects of strain state and strain rate on deformation-induced transformation in 304 stainless steel: Part I. Magnetic measurements and mechanical behavior, Metall. Trans. A. 13 (1982) 619–626.

[24] J. Talonen, H. Hänninen, Formation of shear bands and strain-induced martensite during plastic deformation of metastable austenitic stainless steels, Acta Mater. 55 (2007) 6108–6118.

[25] J.A. Venables, The martensite transformation in stainless steel, Philos. Mag. 7 (1962) 35–44.

[26] R.E. Schramm, R.P. Reed, Stacking fault energies of seven commercial austenitic stainless steels, Metall. Mater. Trans. A. 6 (1975) 1345–1351.

[27] A. Das, Revisiting Stacking Fault Energy of Steels, Metall. Mater. Trans. A. 47 (2016) 748–768. doi:10.1007/s11661-015-3266-9.

[28] H.M. Otte, The formation of stacking faults in austenite and its relation to martensite, Acta Metall. 5 (1957) 614–627.

[29] R.E. Smallman, K.H. Westmacott, Stacking faults in face-centred cubic metals and alloys, Philos. Mag. 2 (1957) 669–683.

[30] B.E. Warren, X-Ray Measurement of Stacking Fault Widths in fcc Metals, J. Appl. Phys. 32 (1961) 2428–2431.

[31] D.E. Mikkola, J.B. Cohen, Effects of Thermal-Mechanical Treatments on Faulting in Some fcc Alloys, J. Appl. Phys. 33 (1962) 892–898.

[32] P.B. Hirsch, H.M. Otte, X-ray diffraction from body-centred cubic crystals containing stacking faults, Acta Crystallogr. 10 (1957) 447–453.

[33] M.S. Paterson, X-ray diffraction by face-centered cubic crystals with deformation faults, J. Appl. Phys. 23 (1952) 805–811.

[34] B.E. Warren, X-ray Diffraction, Courier Corporation, 1969.

[35] K. Warsinski, EVALUATION OF THERMAL STABILITY OF AUSFERRITE IN AUSTEMPERED DUCTILE IRON USING DIFFERENTIAL SCANNING CALORIMETRY, (2017).

[36] T. Ungár, Microstructural parameters from X-ray diffraction peak broadening, Scr. Mater. 51 (2004) 777–781.

[37] K.L. Hayrynen, The production of austempered ductile iron (ADI), in: World Conf. ADI, 2002: pp. 1–6.

[38] C.Y. Kung, J.J. Rayment, An examination of the validity of existing empirical formulae for the calculation of ms temperature, Metall. Trans. A. 13 (1982) 328–331. doi:10.1007/BF02643327.

[39] K.W. Andrews, Empirical formulae for the calculation of some transformation temperatures, J Iron Steel Inst. (1965) 721–727.

[40] A.M. Beese, D. Mohr, Anisotropic plasticity model coupled with Lode angle dependent strain-induced transformation kinetics law, J. Mech. Phys. Solids. 60 (2012) 1922–1940. doi:10.1016/j.jmps.2012.06.009.

[41] A.M. Beese, D. Mohr, Effect of stress triaxiality and Lode angle on the kinetics of strain-induced austenite-to-martensite transformation, Acta Mater. 59 (2011) 2589–2600. doi:10.1016/j.actamat.2010.12.040.

[42] Z.L. Xie, Y. Liu, H. Haenninen, Stabilization of retained austenite due to partial martensitic transformations, Acta Metall. Mater. 42 (1994) 4117–4133.

[43] J.R. Patel, M. Cohen, Criterion for the action of applied stress in the martensitic transformation, Acta Metall. 1 (1953) 531–538.

[44] Z.L. Xie, Y. Liu, H. Hänninen, Stabilization of austenite associated with prior formation of martensite, J. Phys. IV. 5 (1995) C8-333-C8-338.

[45] J.R. Davis, ASM specialty handbook: tool materials, ASM international, 1995.

[46] J.B. Cohen, C.N.J. Wagner, Determination of twin fault probabilities from the diffraction patterns of fcc metals and alloys, J. Appl. Phys. 33 (1962) 2073–2077.

Appendix A: Single Crystallite Intensity Distribution

Following the original derivation from Paterson, the lattice points in an FCC lattice are translated to be represented in hexagonal coordinates, as shown in Figure A.1. The translation done to reorient the sample unit cell to be in line with the close-packed plane (111), so the effects from faulting can be easily elucidated. This creates the A_1 and A_2 directions in the (111) plane, with the A_3 perpendicular to the (111) plane. For the eventual translation to reciprocal space, the indices $H_oK_oL_o$ are used for the hexagonal lattice which are translated from the hkl used in the FCC lattice. These translations are listed in Table A.1.

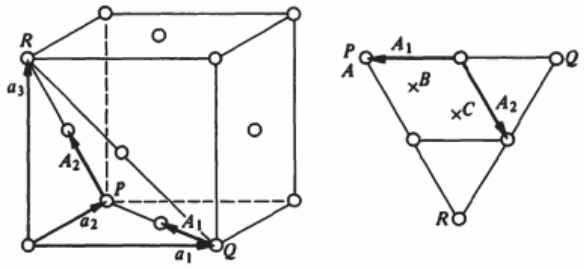

Figure A.1: Visual depiction of the relationship between the FCC lattice and hexagonal lattice points required for the stacking and twin fault calculation. The FCC lattice directions are shown as a_1,a_2,a_3 and they are translated to hexagonal coordinates as A_1,A_2,A_3. The stacking layers, *ABC*, are shown in the hexagonal plane as x points. The *PQR* points in the FCC unit cell correspond to *PQR* points in the hexagonal lattice plane shown on the right.[6]

Using the hexagonal translation, the FCC unit cell can be represented as a unit cell containing 3 total atoms, with one atom per layer. The index m_n is introduced to describe

[6] Reprinted by permission from Dover Publications Inc: X-ray Diffraction, pg. 276, B.E. Warren, 1990. See Appendix F for documentation to republish this material.

the position of an atom in a plane m_3, in real space. The position of a single atom in the (111) plane (FCC) can be described in these hexagonal coordinates as:

$$R_{m_1 m_2 m_3} = m_1 A_1 + m_2 A_2 + \frac{m_3 A_3}{3} + \delta(m_3) \quad \text{(A.1)}$$

Table A.1: Translations for FCC to hexagonal lattice points that are used in the stacking fault and twin fault calculation derivation. The $A_1A_2A_3$ and $H_oK_oL_o$ are the hexagonal coordinates and reciprocal lattice indices, while the a_1,a_2,a_3 and hkl are the FCC coordinates and indices.

$A_1 = \frac{-a_1}{2} + \frac{a_2}{2}$	$H_o = \frac{-h}{2} + \frac{k}{2}$
$A_2 = \frac{-a_2}{2} + \frac{a_3}{2}$	$K_O = \frac{-k}{2} + \frac{l}{2}$
$A_3 = a_1 + a_2 + a_3$	$L_o = h + k + l$

The delta term, $\delta(m_3)$, is the displacement of the layer in the m_3 direction. Using this atom position equation, the intensity from a single crystal is given by Equation A.2. This double sum includes the complex conjugate to calculate the total intensity from the exponential terms. This is the origin of the m' terms (atom) in the second sum in Equation 1.2, and is effectively the same as m. With the $(s-s_o)/\lambda$ representing the diffraction vector, I_e the incident intensity and f_m being the atomic scattering factor for a given atom:

$$I = I_e \sum_m f_m e^{\frac{2\pi i(s-s_o)R_m}{\lambda}} \sum_{m'} f_{m'} e^{\frac{-2\pi i(s-s_o)R_{m'}}{\lambda}} \quad \text{(A.2)}$$

The sums over $m_1 m_2$ and $m'_1 m'_2$, (i.e. the single plane A_1A_2) can be calculated immediately to a constant to narrow down the single crystal intensity equation to being dependent on the m_3 direction, because faulting will affect the atoms in this direction

only. To expand the summation past one unit-cell, the layers are assumed to be parallelograms of dimensions (N_1N_2), where the single layer dimensions are now N_1A_1 and N_2A_2. This constant (sum over $N_1A_1N_2A_2$) is represented as ψ^2 and is equal to Equation A.3. After this term is pulled out from the summation, Equation A.2 becomes Equation A.4

$$\psi^2 = I_e f^2 \frac{\sin^2(\pi/\lambda)(\mathrm{s}-\mathrm{s_o})N_1A_1}{\sin^2(\pi/\lambda)(\mathrm{s}-\mathrm{s_o})A_1} \frac{\sin^2(\pi/\lambda)(\mathrm{s}-\mathrm{s_o})N_2A_2}{\sin^2(\pi/\lambda)(\mathrm{s}-\mathrm{s_o})A_2} \tag{A.3}$$

$$\mathrm{I} = \psi^2 \sum_{\mathrm{m_3}} e^{2\pi i\left\{\frac{\mathrm{s}-\mathrm{s_o}}{\lambda}\right\}*\left\{\frac{m_3A_3}{3}+\delta(m_3)\right\}} \sum_{m_{3'}} e^{-2\pi i\left\{\frac{\mathrm{s}-\mathrm{s_o}}{\lambda}\right\}*\left\{\frac{m_{3'}A_3}{3}+\delta(m_{3'})\right\}} \tag{A.4}$$

To further simply this intensity expression, the diffraction vector can be represented in the reciprocal space vector, $B_1B_2B_3$, following equation A.5, where $h_1h_2h_3$ are continuous variables. These directly relate to the whole integer $H_oK_oL_o$ indices, where the h_1 is parallel to H_o, h_2 is parallel to K_o, and h_3 is parallel to L_o. Three additional abbreviations are used to simplify equation A.4 during the translation to reciprocal space and are given as equations A.6 through A.9. These abbreviations combine the m and m' terms to a single m term, to reduce the summation to one over m. If we assume that $\langle e^{i\phi_m} \rangle$ can represent an average phase difference from layer displacement in the reciprocal lattice over all m*th* neighbor pairs and N_m represent the number of layers with an m*th* neighbor. This eliminates the dual m_3 and $m_{3'}$ position terms that were previously used, and combines them to an average, m.

$$\frac{\mathrm{s}-\mathrm{s_o}}{\lambda} = \mathrm{h_1B_1} + \mathrm{h_2B_2} + \mathrm{h_3B_3} \tag{A.5}$$

$$\mathrm{m} = \mathrm{m_3} - \mathrm{m_{3'}} \tag{A.6}$$

$$\delta(\mathrm{m}) = \delta(\mathrm{m_3}) - \delta(\mathrm{m_{3'}}) \tag{A.7}$$

$$\phi(\mathrm{m}) = 2\pi(\mathrm{h_1B_1} + \mathrm{h_2B_2} + \mathrm{h_3B_3}) * \delta(\mathrm{m}) \tag{A.8}$$

Now the intensity equation is represented as:

$$I = \psi^2 \sum_{m=-\infty}^{\infty} N_m \langle e^{i\phi_m} \rangle e^{\frac{2\pi i m h_3}{3}} \quad (A.9)$$

The first $\langle e^{i\phi(m)} \rangle$ contains the combination $\delta(m)$, which is the displacement in the m_3 layer position, while the second $e^{\frac{2\pi i m h_3}{3}}$ term contains the m layer combination term $m_3 - m_{3'}$, which is determined from the vector perpendicular to the (111) plane.

Appendix B: Reciprocal Space Intensity Distribution

The probability difference functions are derived separately for each specific type of fault, stacking or twin, using Figure B.1a and B.1b respectively.

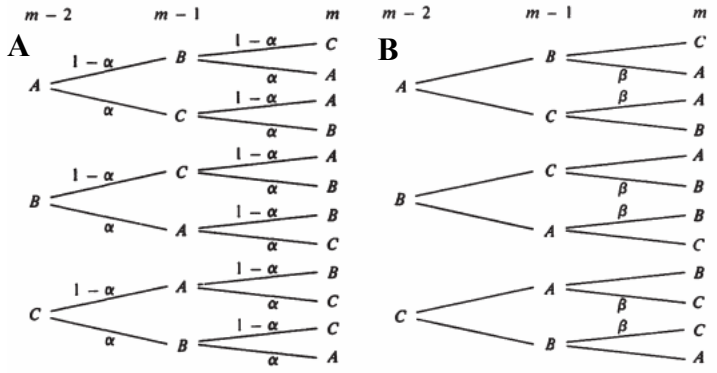

Figure B.1: Probability trees for the FCC stacking sequence for **A)** stacking faults and **B)** twin faults. The α and β terms refer to the probability of a stacking or twin fault respectively.[7]

α is the term associated with the stacking fault probability and β is the term for twin fault probability. If (1-α) is the probability the sequence doesn't indicate a stacking fault, then the probability that an atom is present in the *A* position on an *m*th layer is given as:

$$P_m^A = P_{m-2}^A 2\alpha(1-\alpha) + P_{m-2}^B (1-\alpha)^2 + P_{m-2}^C \alpha^2 \quad \text{(B.1)}$$

Equation B.1 is combined with Equation B.2 to calculate the entire difference equation for stacking faults in FCC materials (eq. B.3), assuming that the sum of the probabilities of finding either an *A*,*B*,*C* positioned layer on the m-2 layer is equal to 1.

$$\mathrm{P}_{\mathrm{m-1}}^{\mathrm{A}} = \mathrm{P}_{\mathrm{m-2}}^{\mathrm{B}}\alpha + \mathrm{P}_{\mathrm{m-2}}^{\mathrm{C}}(1-\alpha) \quad \text{(B.2)}$$

$$\mathrm{P}_{\mathrm{m}}^{\mathrm{A}} + \mathrm{P}_{\mathrm{m-1}}^{\mathrm{A}} + \mathrm{P}_{\mathrm{m-2}}^{\mathrm{A}} = 1 - \alpha - \alpha^2 \quad \text{(B.3)}$$

[7] Reprinted by permission from Dover Publications Inc: X-ray Diffraction, pg. 278, B.E. Warren, 1990. See Appendix F for documentation to republish this material.

Similarly, the difference equation for twin faulting can be derived. In a normal stacking sequence, the next layer should always be different than the preceding two layers (i.e. *AB->C*, or *BC->A*), however if a twin fault is present then this relationship is not valid. When comparing the probability tree in Figure B.1b, the probability of *A* on the m-2 layer (P^{A}_{m-2}) is equal to the combined probability that *A* is followed by *B* in the m-2 and *A* is followed by C in the m-1 layers. It is also follows that the combined probabilities of ($P^{B}_{m-2} + P^{C}_{m-2} - P^{A}_{m-1}$) are equal to the probability of *B* followed by *C* in the m-2 layer and *C* followed by *B* in the m-1 layer. Following the same assumption as the stacking fault probability, that the m-2 must be either *A, B* or *C*, the final difference equation for twin faulting is calculated as:

$$\mathrm{P^{A}_{m}} + \mathrm{P^{A}_{m-1}}(1-\beta) + \mathrm{P^{A}_{m-2}}(1-2\beta) = 1-\beta \tag{B.4}$$

Combining these two probabilities, assuming that they are independent of each other and approximating $\alpha(1-\alpha)$ by using just α, we obtain a combined difference equation:

$$P^{A}_{m} + P^{A}_{m-1}(1-\beta) + P^{A}_{m-2}(1-3\alpha-2\beta) = 1-\alpha-\beta \tag{B.5}$$

To solve this for the required $\mathrm{P^{A}_{m}}$ term that is plugged into the intensity equation, Equation B.5 can be solved using a power form including m ($\mathrm{a + bx^{m}}$), to obtain two solutions. To solve for the boundary conditions for these solution, the $P^{A,B,C}_{m}$ notation is replaced by a more general notation form, $\mathrm{P^{-,0,+}_{m}}$ to represent the probability that an *m*th plane is the same, ahead or behind one step in the sequence when compared to the starting layer. The solved form, with a positive m value, of $\mathrm{P^{0}_{m}}$ is given as Equation B.6.

$$\mathrm{P^{0}_{m}} = \frac{1}{3}\left\{1 + \left[1 - \frac{\beta}{i\sqrt{3-12\alpha-6\beta}}\right]\left[\frac{-(1-\beta)+i\sqrt{3-12\alpha-6\beta}}{2}\right]^{m} + \left[1 + \frac{\beta}{i\sqrt{3-12\alpha-6\beta}}\right]\left[\frac{-(1-\beta)-i\sqrt{3-12\alpha-6\beta}}{2}\right]^{m}\right\} \tag{B.6}$$

Equation B.6 can be simplified, replacing the $\left[\frac{-(1-\beta)+i\sqrt{3-12\alpha-6\beta}}{2}\right]$ term with an exponential term which introduces two new variables Z and γ, and assumes the α^2 and β^2 are zero. The simplification is calculated as:

$$\frac{-(1-\beta)+i\sqrt{3-12\alpha-6\beta}}{2} = Ze^{\pm i\gamma} \approx Z(\cos\gamma \pm i\sin\gamma) \tag{B.7}$$

Where Z and γ are equal to:

$$Z = 1 - 1.5\alpha - \beta \tag{B.8}$$

$$\gamma = \frac{\pi}{3} - \frac{\sqrt{3}\alpha}{2} \tag{B.9}$$

Utilizing the abbreviation from Equation B.7, Equation B.6 for a positive m is now:

$$P_m^0 = \frac{1}{3}\left[1 + 2(-1)^m Z^m\left(\cos m\gamma + \left(\frac{\beta}{s}\right)\sin m\gamma\right)\right] \tag{B.10}$$

For a negative m, it is slightly different:

$$P_m^0 = \frac{1}{3}\left[1 + 2(-1)^m Z^{-m}\left(\cos m\gamma - \left(\frac{\beta}{s}\right)\sin m\gamma\right)\right] \tag{B.11}$$

Equations B.11 and B.12 are the final difference equations that will relate the stacking or twin fault probability to the changes in the intensity distribution. Taking the starting layer to be in position A, then the displacements and phase factor for a *m*th layer will be as shown in Table B.1.

Table B.1: Layer displacements and corresponding reciprocal phase factor for an *m*th layer as calculated from Figure A.1. The -, 0 or + term in each displacement or shift corresponds to the position of each layer relative to the base layer (*A*) in terms of the stacking sequence *ABC* (i.e. + would mean a *B* layer, while – would mean a *C* layer)

$\delta_m^- = \frac{(-A_1 + A_2)}{3}$	$\phi_m^- = \frac{2\pi(h_1 - h_2)}{3}$
$\delta_m^0 = 0$	$\phi_m^0 = 0$
$\delta_m^+ = \frac{(A_1 - A_2)}{3}$	$\phi_m^+ = \frac{-2\pi(h_1 - h_2)}{3}$

Utilizing the reciprocal lattice phase factor given in Table B.1 in determining the average reciprocal space phase factor $\langle e^{i\phi_m} \rangle$, it is calculated as:

$$\langle e^{i\phi m} \rangle = P_m^- \langle e^{i\phi_m^-} \rangle + P_m^0 \langle e^{i\phi_m^0} \rangle + P_m^+ \langle e^{i\phi_m^+} \rangle \quad \text{(B.12)}$$

The average phase factor can be calculated as:

$$\langle e^{i\phi m} \rangle = P_m^0 + (1 - P_m^0)\cos\frac{2\pi(H_o - K_o)}{3} \quad \text{(B.13)}$$

Using this relationship, each unique reflection in a {hkl} family of planes can be determined to be affected or unaffected by faulting. The average phase shift factor of the affected reflections in an {hkl} family of planes can be inserted into the equation for intensity distribution in reciprocal space, given as $\frac{(-1+3P_m^0)}{2}$. Combining both Equations B.11 and B.13, we obtain a general form of the phase shift formula given as:

$$\langle e^{i\phi m} \rangle = (-1)^m Z^{|m|} \left(\cos m\gamma + \left(\frac{\beta}{s}\right) \sin|m|\gamma \right) \quad \text{(B.14)}$$

Inserting the average phase shift from affected reflections into Equation A.9, an updated reciprocal space intensity distribution function is calculated and is given as:

$$I = \psi^2 \sum_{m=-\infty}^{\infty} N_m (-1)^m Z^{|m|} \left(\cos m\gamma + \left(\frac{\beta}{s}\right) \sin|m|\gamma \right) e^{\frac{2\pi i m h_3}{3}} \quad \text{(B.15)}$$

The last exponential term in Equation B.15 can be expanded to the trigonometric form, where the $i \sin \frac{2\pi i m h_3}{3}$ terms cancels out due to orthogonality. Using the relations of $\sin|m|A \cos mB = \sin mA \cos mB$ and $\cos mA = \cos mB$ Equation B.15 becomes:

$$I = \frac{\psi^2}{2} \sum_m N_m Z^{|m|} \left[\cos 2\pi m \left(\frac{h_3 - 1}{3} - \frac{\sqrt{3}\alpha}{4\pi} \right) + \frac{\beta}{\sqrt{3}} \sin 2\pi |m| \left(\frac{h_3 - 1}{3} - \frac{\sqrt{3}\alpha}{4\pi} \right) + \cos 2\pi m \left(\frac{h_3 + 1}{3} + \frac{\sqrt{3}\alpha}{4\pi} \right) - \frac{\beta}{\sqrt{3}} \sin 2\pi |m| \left(\frac{h_3 + 1}{3} + \frac{\sqrt{3}\alpha}{4\pi} \right) \right] \quad \text{(B.16)}$$

If we apply the criterion for affected and unaffected peaks, the cos and sin series in Equation B.17 can be combined to further simplify to:

$$I = \psi^2 \sum_m N_m Z^{|m|} \left[\cos 2\pi m \left(\frac{h_3 - L_o}{3} - (\pm) \frac{\sqrt{3}\alpha}{4\pi} \right) \pm \frac{\beta}{\sqrt{3}} \sin 2\pi |m| \left(\frac{h_3 - L_o}{3} - (\pm) \frac{\sqrt{3}\alpha}{4\pi} \right) \right] \quad \text{(B.18)}$$

Equation B.18 is the final form of the intensity distribution in reciprocal space, as a function of the continuous variables, $h_1 h_2 h_3$.

Appendix C: Real Space Power Distribution and Stacking Fault Probability

To interpret measured diffraction powder patterns, the reciprocal intensity distribution must be translated to real space (2θ) with an integration over all the crystallites in the sample. This will give the power distribution in real space. Figure C.1 illustrates the variation in reciprocal space that corresponds to a change in the diffraction vector, which can be finally translated to real space. The intensity in reciprocal space is spread around the point R ($H_oK_oL_o$), in Figure C.1, where it is spread parallel on the B_3 axis due to the faulting because the Fourier coefficients $Z^{|m|}$ increase with increased faulting levels. It also spreads parallel along the B_1 and B_2 axes dependent on the layer dimensions, N_1A_1 and N_2A_2, however taking the assumption that the faulting is throughout the layer in the crystallite and that the crystallites are of sufficient size that size broadening (the spread of intensity parallel to the B_1 and B_2 axes) is not significant. Therefore, the intensity can be assumed to only spread parallel along the B_3 axis. There is also a shift in the point R to R' from the change in h_3, represented by $B_3\Delta h_3$. This can be related to the diffraction vector $\frac{2\sin\theta}{\lambda}$, with Equation C.1.

$$B_3\Delta h_3 \sin\phi = \Delta\left(\frac{2\sin\theta}{\lambda}\right) = \frac{\cos\theta}{\lambda}\Delta(2\theta) \qquad \text{(C.1)}$$

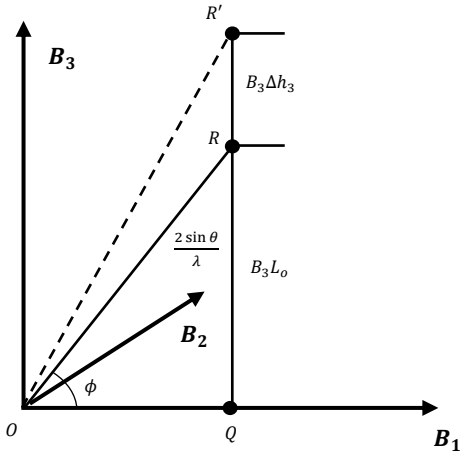

Figure C.1: Representation of reciprocal lattice in terms of the axes B_1B_2 and B_3. The standard lattice point, $H_oK_oL_o$, is represented by R and the shifted point represented by R'. The B_2 axis is pointing into the paper.[8]

The distribution of power in real space is given by the powder pattern theorem, calculated as Equation C.2. Using equation C.1, we can express the dh_3 term in terms of the reciprocal space shift, thus giving the adjusted power distribution in real space in Equation C.3.

$$\int P_{2\theta} d(2\theta) = \frac{I_e M R^2 \lambda^3}{4\upsilon_a} \int\int\int \frac{I(h_1 h_2 h_3)}{\sin\theta} dh_1 dh_2 dh_3 \tag{C.2}$$

$$\int P_{2\theta} d(2\theta) = \frac{M R^2 \lambda^3}{4\upsilon_a} \int\int\int \frac{I(h_1 h_2 h_3)}{\sin\theta} dh_1 dh_2 \frac{\cos\theta d(2\theta)}{\lambda B_3 |\sin\phi|} \tag{C.3}$$

In a fixed diffractometer instrument, this power distribution must be represented in terms of the diffraction circle radius, R, where Equation C.3 must be divided by the term $2\pi R\sin(2\theta)$, which transforms the power distribution into Equation C.4:

$$P'_{2\theta} = \frac{M R \lambda^2}{16\pi 4\upsilon_a B_3 \sin^2\theta |\sin\phi|} \int\int \frac{I(h_1 h_2 h_3)}{\sin\theta} dh_1 dh_2 \tag{C.4}$$

[8] Reprinted by permission from Dover Publications Inc: X-ray Diffraction, pg. 279, B.E. Warren, 1990. See Appendix F for documentation to republish this material.

Recalling that in the reciprocal space intensity distribution, $I(h_1 h_2 h_3)$, the terms that depend on $dh_1 dh_2$ are contained in the constant ψ^2, therefore the integrals may be immediately performed to reduce this down to Equation C.5.

$$\int\int \psi^2 dh_1 dh_2 = I_e f^2 \int\int \frac{\sin^2 N_1 h_1}{(\pi h_1)^2} \frac{\sin^2 N_2 h_2}{(\pi h_2)^2} dh_1 dh_2 = I_e f^2 N_1 N_2 \quad \text{(C.5)}$$

The remaining terms include the summation terms from Equation 1.27 and the constant term in front of the integrals in Equation 1.31. To remove the M term in the constant (number of crystallites), we can let the N_3 term be the average number of (111) layers in a single crystallite and calculate the total number of atoms in the entire sample from $N_t = MN_1N_2N_3$. Therefore, the unit cell volume (υ_a) must be converted to the volume per atom (layer) as $\upsilon_a/3$. This constant now becomes:

$$G = \frac{N_o R \lambda I_e f^2}{16\pi v_o \sin^2 \theta} \quad \text{(C.6)}$$

In addition to this constant, an additional translation is derived from Figure C.1 to combine the affected and unaffected components into one power distribution function. If we assume that the line *RO* is along the b_3 axis in an orthorhombic unit cell, then the diffraction vector can also be represented in terms of a new continuous variable, h_3', along with a new index replacing L_o, l'. Therefore, any (*hkl*) peak measured from the real sample is related to an equivalent (*00l'*) reflection in an orthorhombic unit cell. Following the first representation in Equation C.1, it is also represented by the portion in bold:

$$B_3 \Delta h_3 \sin\phi = \Delta\left(\frac{2\sin\theta}{\lambda}\right) = (\mathbf{h_3'} - \mathbf{l'})\mathbf{b_3'} \quad \text{(C.7)}$$

The $(h_3' - l')$ term is equivalent to the $B_3\Delta h_3$ term in the original representation. Using this new representation to replace the old representation from the reciprocal space distribution derivation, the term $\frac{h_3 - L_o}{3} - (\pm)\frac{\sqrt{3}\alpha}{4\pi}$ is transformed to:

$$\frac{b_3'}{3B_3 \sin\phi}\left[h_3' - l' - (\pm)\frac{\sqrt{3}\alpha 3B_3 \sin\phi}{4\pi b'_3}\right] \quad (C.8)$$

Using this new term for the power distribution gives the updated power distribution equation:

$$P'_{2\theta} = \frac{G}{3B_3 \sin\phi}\sum_m \frac{N_m}{N_3} Z^m \left[\cos 2\pi mq(h_3 - l' - \varepsilon) + (\pm)\frac{\beta}{\sqrt{3}}\sin 2\pi mq(h_3 - l' - \varepsilon)\right] \quad (C.9)$$

$$\varepsilon = \frac{\sqrt{3}\alpha 3B_3 \sin\phi}{4\pi b'_3} \quad (C.10)$$

$$q = \frac{b_3'}{3B_3 \sin\phi} \quad (C.11)$$

If we assume that the $\frac{N_m Z^m}{N_3}$ terms vary slowly with an increasing *m* value (layer), a further simplification can be made to move the q constant given in Equation C.11 out of the trigonometric term into the coefficient terms in Equation C.9. This allows for the power distribution equation to be applied to both affected and unaffected reflections by reducing the variable terms in the trig functions to one combined variable, n, where n=*m*q. Take a single function:

$$\sum_m \frac{N_m Z^m}{N_3}\cos 2\pi mqx \quad (C.12)$$

Which is equivalent a single cos function pulled from Equation C.9, where $x = (h_3 - l' - \varepsilon)$. If the coefficient terms vary slowly with *m*, we can replace the summation with an integral and introduce the new quantity, n=*m*q (m=n/q):

$$\int \frac{N_m Z^m}{N_3}\cos 2\pi mqx \ dm \rightarrow \frac{1}{|q|}\int \frac{N_{n/q} Z^{n/q}}{N_3}\cos 2\pi nx \ dn \quad (C.13)$$

Now, we can convert this modified integral back to a summation over m for the power equation:

$$\int \frac{N_{n/q} Z^{n/q}}{N_3} \cos 2\pi nx \; dn \rightarrow \frac{1}{|q|} \sum_m \frac{N_{n/q} Z^{n/q}}{N_3} \cos 2\pi nx \tag{C.14}$$

This relation can also be used to modify the sin term, to remove the q quantity. With these modified summations, the final power distribution equation for one single reflection is:

$$P'_{2\theta} = \frac{G}{b'_3} \sum_n \frac{N_{n/q}}{N_3} Z^{n/q} \left[\cos 2\pi n(h_3 - l' - \varepsilon) + (\pm) \frac{\beta}{\sqrt{3}} \sin 2\pi |n| (h_3 - l' - \varepsilon) \right] \tag{C.15}$$

Note that the total summation is now over n, which is equal to *m*q. To add the total contributions to the power distribution over an entire $\{hkl\}$ family to calculate the $P'_{2\theta}(h_o)$, additional summations to add the affected and unaffected components together must be made. Equation C.15 is the power distribution function for a peak that is **affected** by faulting. For an **unaffected** peak, where ($Z^{n/q}$=1, ε=0 and β=0) Equation C.15 becomes:

$$P'_{2\theta} = \frac{G}{b'_3} \sum_n \frac{N_{n/q}}{N_3} [\cos 2\pi n(h_3 - l')] \tag{C.16}$$

Combining these two equations into one total power distribution function, dependent on a single $\{hkl\}$ family yields:

$$P'_{2\theta}\{hkl\} = \frac{G}{b'_3} \sum_n \left[\sum_a \frac{N_{n/q}}{N_3} Z^{n/q} \cos 2\pi n(h_3 - l' - \varepsilon) + \sum_u \cos 2\pi n(h_3 - l') + \frac{\beta}{\sqrt{3}} \sum_a \frac{N_{n/q}}{N_3} Z^{n/q} (\pm) \sin 2\pi |n| (h_3 - l' - \varepsilon) \right] \tag{C.17}$$

The two cos terms can be approximated to be equal to one single cos term, producing a term that has an average coefficient (broadening) and displacement (shift). The displacement term (ε) can also be approximated to be equal for both the sin and cos terms, due to the sin term having a very small coefficient $\left(\frac{\beta}{\sqrt{3}}\right)$. Using these modifications, the

coefficient terms can be pulled out for the sin and cos terms, along with a single displacement term to yield:

$$P'_{2\theta}\{hkl\} = \frac{G(u+a)}{b'_3}\sum_n[A_n \cos 2\pi n(h_3 - l' - \delta) + B_n \sin 2\pi n(h_3 - l' - \delta)] \quad (C.18)$$

$$A_n = \left(\frac{1}{u+a}\right)\left[\sum_a \frac{N_{n/q}}{N_3} Z^{n/q} + \sum_u \frac{N_{n/q}}{N_3}\right] \quad (C.19)$$

$$B_n = \left(\frac{1}{u+a}\right)\left[\frac{\beta}{\sqrt{3}}\sum_a \frac{N_{n/q}}{N_3} Z^{n/q}(\pm)\frac{L_o}{|L_o|}\right] \quad (C.20)$$

$$\delta = \left(\frac{1}{u+a}\right)\left[\frac{3\sqrt{3}\alpha B_3}{4\pi b'_3}\right]\sum_a(\pm)\sin\phi \quad (C.21)$$

Equation C.18 represents the final power distribution function, from which stacking and twin fault probabilities may be derived. Broadening of the total $\{hkl\}$ reflection is dependent on the sin term, which is proportional to the β (twin fault probability) term, but also depends on the Z term which is dependent on both α (stacking fault probability) and β. A shift in the position (Δh_3) from the displacement term, δ, is directly related to α and is the origin of the peak shift relation used in this work. To calculate the real-space 2θ shift that occurs from the presence of stacking faults, the relation established with Equation C.1 is used to represent the change in diffraction vector in terms of the delta term given in Equation C.21.

$$\Delta\left(\frac{2\sin\theta}{\lambda}\right) = (h'_3 - l')b'_3 \rightarrow \Delta 2\theta = \frac{\lambda b'_3 \delta}{\cos\theta} \quad (C.22)$$

Inserting the displacement term (Equation C.21) we obtain a general form for the peak shift as a function of stacking fault probability

$$\Delta 2\theta = \left[\frac{3\sqrt{3}\alpha B_3 \lambda}{4\pi(u+a)\cos\theta}\right]\sum_a(\pm)\sin\phi \quad (C.23)$$

Following Figure C.1, the reciprocal space terms can be related to the real space lattice dimensions and indices. The $\sin\phi$ term can be directly related to the interplanar spacing, d, of the material with $\sin\phi = B_3 L_o d$. This modified equation is now equal to:

$$\Delta 2\theta = \left[\frac{3\sqrt{3}\alpha B_3^2 \lambda d}{4\pi(u+a)\cos\theta}\right]\sum_a(\pm)\, L_o \tag{C.24}$$

With the B_3^2 term (reciprocal space vector) being equivalent to Equation C.25, with a being the cubic cell lattice parameter. By also replacing λ with 2dsinθ (Bragg law) we obtain Equation C.26.

$$B_3^2 = \frac{1}{A_3^2} = \frac{1}{3a^2} \tag{C.25}$$

$$\Delta 2\theta = \left[\frac{6\sqrt{3}\alpha\frac{1}{3a^2}\sin\theta d^2}{\pi(u+a)\cos\theta}\right]\sum_a(\pm)\, L_o \tag{C.26}$$

The a^2 term can be replaced with $d^2 h_o^2$ where $h_o^2 = \sqrt{h^2 + k^2 + l^2}$ (in cubic unit cell). Now Equation C.26 reduces to:

$$\Delta 2\theta = \left[\frac{6\sqrt{3}\alpha\frac{1}{3h_o^2}\sin\theta}{4\pi(u+a)\cos\theta}\right]\sum_a(\pm)\, L_o \rightarrow \left[\frac{\sqrt{3}\alpha\tan\theta}{2\pi h_o^2(u+a)}\right]\sum_a(\pm)\, L_o \tag{C.27}$$

Finally, multiplying by 180/π to convert from radians to degrees gives the final peak shift equation as a function of stacking fault probability.

$$\Delta 2\theta = \left[\frac{90\sqrt{3}\alpha\tan\theta}{\pi^2 h_o^2(u+a)}\right]\sum_a(\pm)\, L_o \tag{C.28}$$

Equation C.28 can be applied to any {*hkl*} family to determine the peak shift from stacking faults. For each family of planes, the constant must be calculated:

$$\frac{1}{h_o^2(u+a)}\sum_a(\pm)\, L_o \tag{C.29}$$

Where the L_o value must be calculated for each individual affected peak following the criterion, $L_o = 3b \pm 1$. The $\tan\theta^o_{hkl}$ refers to the standard, non-broadened peak position as it is derived from the original, unaffected lattice. For the {111} family, the h_o^2 is equal to 3, and the total number of reflections in the family is 8. Similarly, for the {200} family the h_o^2 is equal to 4, and the total number of reflections in the family is 6. The full list of values used in the summation term is listed in Table C.1. Therefore, the peak shift equations for {111} and {200} peaks are calculated from Equations C.30 and C.31 respectively.

$$\Delta 2\theta = \left[\frac{90\sqrt{3}\alpha \tan\theta^o_{111}}{\pi^2}\right](0.25) \tag{C.30}$$

$$\Delta 2\theta = \left[\frac{90\sqrt{3}\alpha \tan\theta^o_{200}}{\pi^2}\right](-0.5) \tag{C.31}$$

Table C.1: Calculated L_o and $\pm$ values from the criterion for determining if a peak will be affected or unaffected by faulting. An affected peak will follow the criterion $L_o = 3b \pm 1$, where unaffected peaks follow $L_o = 3b$. The L_o term is calculated directly $L_o = h + k + l$ relation given in Table 1.1.

{111}	L_o	(±)	{200}	L_o	(±)
(111)	3	0	(200)	2	-
(11-1)	1	+	(020)	2	-
(1-11)	1	+	(002)	2	-
(-111)	1	+	(-200)	-2	+
(-1-11)	-1	-	(0-20)	-2	+
(-11-1)	-1	-	(00-2)	-2	+
(1-1-1)	-1	-			
(-1-1-1)	-3	0			

The change in the difference between two peaks may also be used, through a combination of two separate single peak shifts. For the (200-111) shift, the change in peak difference between these two peaks can be calculated with Equation C.32.

$$\Delta(2\theta_{200} - 2\theta_{111})^\circ = \frac{-90\sqrt{3}\alpha}{\pi^2}\left[\frac{\tan\theta_{200}}{2} + \frac{\tan\theta_{111}}{4}\right] \quad \text{(C.32)}$$

Appendix D: Twin Fault Probability

As seen in equation C.20, the sin term coefficient B_n is directly dependent on β, thus the peak broadening from the sin term is directly related to this probability. It was shown by Cohen and Wagner that the associated center of gravity (centroid) shift of a given reflection compared to the peak maxima can be related to the twin fault probability, β, if we assume that no other sources of faulting or peak asymmetry exists.[46]

The centroid shift from the peak maxima can be calculated using the following relation:

$$\Delta CG = \frac{\int h_3 P'_{2\theta}(h_3) dh_3}{\int P'_{2\theta}(h_3) dh_3} \quad (D.1)$$

Where the $P'_{2\theta}$ is the power distribution function from Equation C.18, and h_3 is equal to the $(h_3 - l' - \delta)$ term in Equation C.18. If we assume that no other faulting is present, this calculation simplifies to:

$$\Delta CG = \frac{-1}{2\pi} \sum_n (-1)^n \frac{B_n}{n} \quad (D.2)$$

Now if we substitute Equation C.20 for B_n and evaluate the sum over infinite n values we obtain Equation D.3, assuming infinitely large crystallites ($(s-s_o) << \lambda$).

$$\Delta CG = \frac{\beta a}{\sqrt{3}\pi(u+a)} (\pm) \frac{L_o}{|L_o|} \quad (D.3)$$

Following the same convention that was used in the stacking fault peak shift derivation to convert the centroid shift to real space, we obtain the final centroid shift equation for any $\{hkl\}$ family. The a term is the number of affected reflections and u is the number of unaffected reflections in any given $\{hkl\}$ family, while the L_o term is calculated following the relation given in Table A.1 and is the same value listed in Table C.1. The

θ^0_{hkl} value is the peak maxima position from an annealed sample, assumed to have zero twin faulting present.

$$\Delta \mathrm{CG} = \frac{360 \ln 2a}{\pi^2\sqrt{3}(u+a)} (\pm) \frac{L_o}{|L_o|} \beta \tan \theta^0_{hkl} \tag{D.4}$$

For the direct calculation, Equation D.4 may be solved out to simplify for single reflections.

$$\Delta \mathrm{CG}_{111} = \frac{360 \ln 2*6}{\pi^2\sqrt{3}(8)} * \frac{6}{6} \beta \tan \theta = 11\beta \tan \theta^o_{111} \tag{D.5}$$

$$\Delta \mathrm{CG}_{200} = \frac{360 \ln 2*3}{\pi^2\sqrt{3}(6)} * \frac{12}{6} \beta \tan \theta = 14.6\beta \tan \theta^o_{200} \tag{D.6}$$

Combining these two equations to analyze two peak centroid shifts in a single calculation yields the equation for the twin-fault probability:

$$\beta = \frac{\Delta(2\theta^{CG}_{111} - 2\theta^{max}_{111}) - \Delta(2\theta^{CG}_{200} - 2\theta^{max}_{200})}{(11 \tan \theta^0_{111} + 14.6 \tan \theta^0_{200})} \tag{D.7}$$

Appendix E: Error Propagation

Standard errors calculated from replicate measurements from the (111) peak position for each type of sample were propagated through for each method of stacking and twin fault calculation. For single peak stacking fault calculation, the error was calculated following:

$$\delta\alpha[\text{single peak}] = \sqrt{\left(\left(\frac{\partial\alpha}{\partial\Delta(2\theta_{hkl})}\right) * \left(\delta\Delta(2\theta_{hkl})\right)\right)^2 + \left(\left(\frac{\partial\alpha}{\partial\theta_{hkl}}\right) * \left(\delta\theta_{hkl}\right)\right)^2} \quad \text{(A.1)}$$

with the partials listed below. The summation term is considered a constant for each unique *HKL*.

$$\left(\frac{\partial\alpha}{\partial\Delta(2\theta_{hkl})}\right) = \frac{\pi^2 \cot\theta_{hkl}}{90\sqrt{3}} \sum_b \left((\pm)\frac{L_o}{h_o^2(u+b)}\right) \quad \text{(A.2)}$$

$$\left(\frac{\partial\alpha}{\partial\theta_{hkl}}\right) = \frac{\pi^2 \Delta 2\theta_{hkl} \csc^2\theta_{hkl}}{90\sqrt{3}} \sum_b \left((\pm)\frac{L_o}{h_o^2(u+b)}\right) \quad \text{(A.3)}$$

For the double peak analysis, in addition to the single peak errors the error in double peak change is also included and the total error was calculated following:

$$\delta\alpha[\text{double peak}] = \sqrt{\left(\left(\frac{\partial\alpha}{\partial\Delta(2\theta_{200}-2\theta_{111})}\right) * \left(\delta(\Delta(2\theta_{200}-2\theta_{111}))\right)\right)^2 + \left(\left(\frac{\partial\alpha}{\partial\theta_{200}}\right) * \left(\delta\theta_{200}\right)\right)^2 + \left(\left(\frac{\partial\alpha}{\partial\theta_{111}}\right) * \left(\delta\theta_{111}\right)\right)^2} \quad \text{(A.4)}$$

with the partials listed below. The summation term that was present in the single peak analysis was calculated and is included in the partials directly.

$$\left(\frac{\partial\alpha}{\partial\Delta(2\theta_{200}-2\theta_{111})}\right) = \frac{\pi^2}{90\sqrt{3}\left(\frac{\tan\theta_{200}}{2}+\frac{\tan\theta_{111}}{4}\right)} \quad \text{(A.5)}$$

$$\left(\frac{\partial\alpha}{\partial\theta_{200}}\right) = \frac{-\pi^2\Delta(2\theta_{200}-2\theta_{111})\sec^2\theta_{200}}{180\sqrt{3}\left(\frac{\tan\theta_{200}}{2}+\frac{\tan\theta_{111}}{4}\right)^2} \quad \text{(A.6)}$$

$$\left(\frac{\partial\alpha}{\partial\theta_{111}}\right) = \frac{-\pi^2\Delta(2\theta_{200}-2\theta_{111})\sec^2\theta_{111}}{360\sqrt{3}\left(\frac{\tan\theta_{200}}{2}+\frac{\tan\theta_{111}}{4}\right)^2} \quad \text{(A.7)}$$

The twin fault probability error was calculated utilizing the errors included both singular peak maxima positions and singular peak centroid shifts from the maxima following the same procedure as the stacking fault probabilities. The double peak (200-111) reflection error was calculated as:

$$\delta\beta[\text{double peak}] = \sqrt{\left(\partial\beta 1 * \delta\left(\Delta\left(2\theta_{111}^{CG} - 2\theta_{111}^{max}\right)\right)\right)^2 + \left(\partial\beta 2 * \delta\left(\Delta\left(2\theta_{200}^{CG} - 2\theta_{200}^{max}\right)\right)\right)^2 + \left(\frac{\partial\beta}{\partial\theta_{111}} * \delta\theta_{111}\right)^2 + \left(\frac{\partial\beta}{\partial\theta_{200}} * \delta\theta_{200}\right)^2} \quad \text{(A.8)}$$

With the partials being listed in equations A.9 through A.12 below:

$$\partial\beta 1 = \frac{\partial\beta}{\partial\Delta\left(2\theta_{111}^{CG} - 2\theta_{111}^{max}\right)} = \frac{1}{(11\tan\theta_{111} + 14.6\tan\theta_{200})} \quad \text{(A.9)}$$

$$\partial\beta 2 = \frac{\partial\beta}{\partial\Delta\left(2\theta_{200}^{CG} - 2\theta_{200}^{max}\right)} = \frac{-1}{(11\tan\theta_{111} + 14.6\tan\theta_{200})} \quad \text{(A.10)}$$

$$\frac{\partial\beta}{\partial\theta_{111}} = \frac{11\left(\Delta\left(2\theta_{111}^{CG} - 2\theta_{111}^{max}\right) - \Delta\left(2\theta_{200}^{CG} - 2\theta_{200}^{max}\right)\right)\sec^2\theta_{111}}{(11\tan\theta_{111} + 14.6\tan\theta_{200})^2} \quad \text{(A.11)}$$

$$\frac{\partial\beta}{\partial\theta_{200}} = \frac{-14.6\left(\Delta\left(2\theta_{111}^{CG} - 2\theta_{111}^{max}\right) - \Delta\left(2\theta_{200}^{CG} - 2\theta_{200}^{max}\right)\right)\sec^2\theta_{200}}{(11\tan\theta_{111} + 14.6\tan\theta_{200})^2} \quad \text{(A.12)}$$

Appendix F: Copyright Clearance Agreements

Copyright agreement for Figure 1.2 in Section 1.1

SPRINGER NATURE LICENSE TERMS AND CONDITIONS

Jan 21, 2018

This Agreement between Nathan Peterson ("You") and Springer Nature ("Springer Nature") consists of your license details and the terms and conditions provided by Springer Nature and Copyright Clearance Center.

License Number	4273891276842
License date	Jan 21, 2018
Licensed Content Publisher	Springer Nature
Licensed Content Publication	Metallurgical transactions, A, Physical metallurgy and materials science
Licensed Content Title	A general mechanism of martensitic nucleation: Part II. FCC → BCC and other martensitic transformations
Licensed Content Author	G. B. Olson, Morris Cohen
Licensed Content Date	Jan 1, 1976
Licensed Content Volume	7
Licensed Content Issue	12
Type of Use	Thesis/Dissertation
Requestor type	academic/university or research institute
Format	print and electronic
Portion	figures/tables/illustrations
Number of figures/tables/illustrations	1
Will you be translating?	no
Circulation/distribution	<501
Author of this Springer Nature content	no
Title	Measurement of Planar Fault Probabilities in Austempered Ductile Iron and 304L Stainless Steel
Instructor name	n/a
Institution name	n/a
Expected presentation date	May 2018
Portions	Figure 5
Requestor Location	Nathan Peterson [redacted] United States Attn: Nathan Peterson
Billing Type	Invoice
Billing Address	[redacted] United States Attn: Nathan Peterson
Total	**0.00 USD**
Terms and Conditions	

Springer Nature Terms and Conditions for RightsLink Permissions

Springer Customer Service Centre GmbH (the Licensor) hereby grants you a non-exclusive, world-wide licence to reproduce the material and for the purpose and requirements specified in the attached copy of your order form, and for no other use, subject to the conditions below:

1. The Licensor warrants that it has, to the best of its knowledge, the rights to license reuse of this material. However, you should ensure that the material you are requesting is original to the Licensor and does not carry the copyright of another entity (as credited in the published version).

   If the credit line on any part of the material you have requested indicates that it was reprinted or adapted with permission from another source, then you should also seek permission from that source to reuse the material.

2. Where **print only** permission has been granted for a fee, separate permission must be obtained for any additional electronic re-use.

3. Permission granted **free of charge** for material in print is also usually granted for any electronic version of that work, provided that the material is incidental to your work as a whole and that the electronic version is essentially equivalent to, or substitutes for, the print version.

4. A licence for 'post on a website' is valid for 12 months from the licence date. This licence does not cover use of full text articles on websites.

5. Where **'reuse in a dissertation/thesis'** has been selected the following terms apply: Print rights for up to 100 copies, electronic rights for use only on a personal website or institutional repository as defined by the Sherpa guideline (www.sherpa.ac.uk/romeo/).

6. Permission granted for books and journals is granted for the lifetime of the first edition and does not apply to second and subsequent editions (except where the first edition permission was granted free of charge or for signatories to the STM Permissions Guidelines http://www.stm-assoc.org/copyright-legal-affairs/permissions/permissions-guidelines/), and does not apply for editions in other languages unless additional translation rights have been granted separately in the licence.

7. Rights for additional components such as custom editions and derivatives require additional permission and may be subject to an additional fee. Please apply to Journalpermissions@springernature.com/bookpermissions@springernature.com for these rights.

8. The Licensor's permission must be acknowledged next to the licensed material in print. In electronic form, this acknowledgement must be visible at the same time as the figures/tables/illustrations or abstract, and must be hyperlinked to the journal/book's homepage. Our required acknowledgement format is in the Appendix below.

9. Use of the material for incidental promotional use, minor editing privileges (this does not include cropping, adapting, omitting material or any other changes that affect the meaning, intention or moral rights of the author) and copies for the disabled are permitted under this licence.

10. Minor adaptations of single figures (changes of format, colour and style) do not require the Licensor's approval. However, the adaptation should be credited as shown in Appendix below.

Appendix — Acknowledgements:

For Journal Content:
Reprinted by permission from **[the Licensor]**: **[Journal Publisher** (e.g. Nature/Springer/Palgrave)] **[JOURNAL NAME]** **[REFERENCE CITATION** (Article name, Author(s) Name), **[COPYRIGHT]** (year of publication)

For **Advance Online Publication papers:**
Reprinted by permission from **[the Licensor]**: **[Journal Publisher** (e.g. Nature/Springer/Palgrave)] **[JOURNAL NAME]** **[REFERENCE CITATION** (Article name, Author(s) Name), **[COPYRIGHT]** (year of publication), advance online publication, day month year (doi: 10.1038/sj.[JOURNAL ACRONYM].)

For Adaptations/Translations:
Adapted/Translated by permission from **[the Licensor]**: **[Journal Publisher** (e.g. Nature/Springer/Palgrave)] **[JOURNAL NAME]** **[REFERENCE CITATION** (Article name, Author(s) Name), **[COPYRIGHT]** (year of publication)

Note: For any republication from the British Journal of Cancer, the following credit line style applies:

Reprinted/adapted/translated by permission from **[the Licensor]**: on behalf of Cancer Research UK: : **[Journal Publisher** (e.g. Nature/Springer/Palgrave)] **[JOURNAL NAME] [REFERENCE CITATION** (Article name, Author(s) Name), **[COPYRIGHT]** (year of publication)

For **Advance Online Publication** papers:
Reprinted by permission from The **[the Licensor]**: on behalf of Cancer Research UK: **[Journal Publisher** (e.g. Nature/Springer/Palgrave)] **[JOURNAL NAME] [REFERENCE CITATION** (Article name, Author(s) Name), **[COPYRIGHT]** (year of publication), advance online publication, day month year (doi: 10.1038/sj.[JOURNAL ACRONYM])

For Book content:
Reprinted/adapted by permission from **[the Licensor]**: **[Book Publisher** (e.g. Palgrave Macmillan, Springer etc) **[Book Title]** by **[Book author**(s)] **[COPYRIGHT]** (year of publication)

Other Conditions:

Version 1.0

Questions? customercare@copyright.com or +1-855-239-3415 (toll free in the US) or +1-978-646-2777.

Copyright agreement for Figure 1.4 in Section 1.2.1

Cengage Learning SO LICENSE TERMS AND CONDITIONS

Jan 21, 2018

This is a License Agreement between Nathan Peterson ("You") and Cengage Learning SO ("Cengage Learning SO") provided by Copyright Clearance Center ("CCC"). The license consists of your order details, the terms and conditions provided by Cengage Learning SO, and the payment terms and conditions.

All payments must be made in full to CCC. For payment instructions, please see information listed at the bottom of this form.

License Number	4272060606061
License date	Jan 17, 2018
Licensed content publisher	Cengage Learning SO
Licensed content title	Physical metallurgy principles
Licensed content date	Jan 1, 1992
Type of Use	Thesis/Dissertation
Requestor type	Academic institution
Format	Print, Electronic
Portion	chart/graph/table/figure
Number of charts/graphs/tables/figures	1
The requesting person/organization is:	Nathan Peterson/Michigan Technological University
Title or numeric reference of the portion(s)	Figure 4.24
Title of the article or chapter the portion is from	4.5 Dislocations in the Face-Centered Cubic Lattice
Editor of portion(s)	N/A
Author of portion(s)	Reza Abbaschian, Robert E. Reed-Hill
Volume of serial or monograph.	N/A
Page range of the portion	98
Publication date of portion	1992
Rights for	Main product
Duration of use	Life of current edition
Creation of copies for the disabled	no
With minor editing privileges	no
For distribution to	United States
In the following language(s)	Original language of publication
With incidental promotional use	no
The lifetime unit quantity of	Up to 499

new product	
Title	Measurement of Planar Fault Probabilities in Austempered Ductile Iron and 304L Stainless Steel
Instructor name	n/a
Institution name	n/a
Expected presentation date	May 2018
Billing Type	Invoice
Billing Address	Nathan Peterson [redacted] United States Attn: Nathan Peterson
Total (may include CCC user fee)	0.00 USD

Terms and Conditions

TERMS AND CONDITIONS

The following terms are individual to this publisher:

Amounts of material. No more than 10% of a single Cengage product may be re-used in your upcoming product. Total Cengage Learning content must equal 10% or less of your upcoming product. If using more than what is permitted by Cengage Learning your permission will automatically be null and void.

Other Terms and Conditions:

STANDARD TERMS AND CONDITIONS

1. Description of Service; Defined Terms. This Republication License enables the User to obtain licenses for republication of one or more copyrighted works as described in detail on the relevant Order Confirmation (the "Work(s)"). Copyright Clearance Center, Inc. ("CCC") grants licenses through the Service on behalf of the rightsholder identified on the Order Confirmation (the "Rightsholder"). "Republication", as used herein, generally means the inclusion of a Work, in whole or in part, in a new work or works, also as described on the Order Confirmation. "User", as used herein, means the person or entity making such republication.

2. The terms set forth in the relevant Order Confirmation, and any terms set by the Rightsholder with respect to a particular Work, govern the terms of use of Works in connection with the Service. By using the Service, the person transacting for a republication license on behalf of the User represents and warrants that he/she/it (a) has been duly authorized by the User to accept, and hereby does accept, all such terms and conditions on behalf of User, and (b) shall inform User of all such terms and conditions. In the event such person is a "freelancer" or other third party independent of User and CCC, such party shall be deemed jointly a "User" for purposes of these terms and conditions. In any event, User shall be deemed to have accepted and agreed to all such terms and conditions if User republishes the Work in any fashion.

3. Scope of License; Limitations and Obligations.

3.1 All Works and all rights therein, including copyright rights, remain the sole and exclusive property of the Rightsholder. The license created by the exchange of an Order Confirmation (and/or any invoice) and payment by User of the full amount set forth on that document includes only those rights expressly set forth in the Order Confirmation and in these terms and conditions, and conveys no other rights in the Work(s) to User. All rights not expressly granted are hereby reserved.

3.2 General Payment Terms: You may pay by credit card or through an account with us payable at the end of the month. If you and we agree that you may establish a standing

account with CCC, then the following terms apply: Remit Payment to: Copyright Clearance Center, 29118 Network Place, Chicago, IL 60673-1291. Payments Due: Invoices are payable upon their delivery to you (or upon our notice to you that they are available to you for downloading). After 30 days, outstanding amounts will be subject to a service charge of 1-1/2% per month or, if less, the maximum rate allowed by applicable law. Unless otherwise specifically set forth in the Order Confirmation or in a separate written agreement signed by CCC, invoices are due and payable on "net 30" terms. While User may exercise the rights licensed immediately upon issuance of the Order Confirmation, the license is automatically revoked and is null and void, as if it had never been issued, if complete payment for the license is not received on a timely basis either from User directly or through a payment agent, such as a credit card company.

3.3 Unless otherwise provided in the Order Confirmation, any grant of rights to User (i) is "one-time" (including the editions and product family specified in the license), (ii) is non-exclusive and non-transferable and (iii) is subject to any and all limitations and restrictions (such as, but not limited to, limitations on duration of use or circulation) included in the Order Confirmation or invoice and/or in these terms and conditions. Upon completion of the licensed use, User shall either secure a new permission for further use of the Work(s) or immediately cease any new use of the Work(s) and shall render inaccessible (such as by deleting or by removing or severing links or other locators) any further copies of the Work (except for copies printed on paper in accordance with this license and still in User's stock at the end of such period).

3.4 In the event that the material for which a republication license is sought includes third party materials (such as photographs, illustrations, graphs, inserts and similar materials) which are identified in such material as having been used by permission, User is responsible for identifying, and seeking separate licenses (under this Service or otherwise) for, any of such third party materials; without a separate license, such third party materials may not be used.

3.5 Use of proper copyright notice for a Work is required as a condition of any license granted under the Service. Unless otherwise provided in the Order Confirmation, a proper copyright notice will read substantially as follows: "Republished with permission of [Rightsholder's name], from [Work's title, author, volume, edition number and year of copyright]; permission conveyed through Copyright Clearance Center, Inc. " Such notice must be provided in a reasonably legible font size and must be placed either immediately adjacent to the Work as used (for example, as part of a by-line or footnote but not as a separate electronic link) or in the place where substantially all other credits or notices for the new work containing the republished Work are located. Failure to include the required notice results in loss to the Rightsholder and CCC, and the User shall be liable to pay liquidated damages for each such failure equal to twice the use fee specified in the Order Confirmation, in addition to the use fee itself and any other fees and charges specified.

3.6 User may only make alterations to the Work if and as expressly set forth in the Order Confirmation. No Work may be used in any way that is defamatory, violates the rights of third parties (including such third parties' rights of copyright, privacy, publicity, or other tangible or intangible property), or is otherwise illegal, sexually explicit or obscene. In addition, User may not conjoin a Work with any other material that may result in damage to the reputation of the Rightsholder. User agrees to inform CCC if it becomes aware of any infringement of any rights in a Work and to cooperate with any reasonable request of CCC or the Rightsholder in connection therewith.

4. Indemnity. User hereby indemnifies and agrees to defend the Rightsholder and CCC, and their respective employees and directors, against all claims, liability, damages, costs and expenses, including legal fees and expenses, arising out of any use of a Work beyond the scope of the rights granted herein, or any use of a Work which has been altered in any unauthorized way by User, including claims of defamation or infringement of rights of copyright, publicity, privacy or other tangible or intangible property.

5. Limitation of Liability. UNDER NO CIRCUMSTANCES WILL CCC OR THE RIGHTSHOLDER BE LIABLE FOR ANY DIRECT, INDIRECT, CONSEQUENTIAL OR INCIDENTAL DAMAGES (INCLUDING WITHOUT LIMITATION DAMAGES FOR LOSS OF BUSINESS PROFITS OR INFORMATION, OR FOR BUSINESS INTERRUPTION) ARISING OUT OF THE USE OR INABILITY TO USE A WORK, EVEN IF ONE OF THEM HAS BEEN ADVISED OF THE POSSIBILITY OF SUCH DAMAGES. In any event, the total liability of the Rightsholder and CCC (including their respective employees and directors) shall not exceed the total amount actually paid by User for this license. User assumes full liability for the actions and omissions of its principals, employees, agents, affiliates, successors and assigns.

6. Limited Warranties. THE WORK(S) AND RIGHT(S) ARE PROVIDED "AS IS". CCC HAS THE RIGHT TO GRANT TO USER THE RIGHTS GRANTED IN THE ORDER CONFIRMATION DOCUMENT. CCC AND THE RIGHTSHOLDER DISCLAIM ALL OTHER WARRANTIES RELATING TO THE WORK(S) AND RIGHT(S), EITHER EXPRESS OR IMPLIED, INCLUDING WITHOUT LIMITATION IMPLIED WARRANTIES OF MERCHANTABILITY OR FITNESS FOR A PARTICULAR PURPOSE. ADDITIONAL RIGHTS MAY BE REQUIRED TO USE ILLUSTRATIONS, GRAPHS, PHOTOGRAPHS, ABSTRACTS, INSERTS OR OTHER PORTIONS OF THE WORK (AS OPPOSED TO THE ENTIRE WORK) IN A MANNER CONTEMPLATED BY USER; USER UNDERSTANDS AND AGREES THAT NEITHER CCC NOR THE RIGHTSHOLDER MAY HAVE SUCH ADDITIONAL RIGHTS TO GRANT.

7. Effect of Breach. Any failure by User to pay any amount when due, or any use by User of a Work beyond the scope of the license set forth in the Order Confirmation and/or these terms and conditions, shall be a material breach of the license created by the Order Confirmation and these terms and conditions. Any breach not cured within 30 days of written notice thereof shall result in immediate termination of such license without further notice. Any unauthorized (but licensable) use of a Work that is terminated immediately upon notice thereof may be liquidated by payment of the Rightsholder's ordinary license price therefor; any unauthorized (and unlicensable) use that is not terminated immediately for any reason (including, for example, because materials containing the Work cannot reasonably be recalled) will be subject to all remedies available at law or in equity, but in no event to a payment of less than three times the Rightsholder's ordinary license price for the most closely analogous licensable use plus Rightsholder's and/or CCC's costs and expenses incurred in collecting such payment.

8. **Miscellaneous.**

8.1 User acknowledges that CCC may, from time to time, make changes or additions to the Service or to these terms and conditions, and CCC reserves the right to send notice to the User by electronic mail or otherwise for the purposes of notifying User of such changes or additions; provided that any such changes or additions shall not apply to permissions already secured and paid for.

8.2 Use of User-related information collected through the Service is governed by CCC's privacy policy, available online here:
http://www.copyright.com/content/cc3/en/tools/footer/privacypolicy.html.

8.3 The licensing transaction described in the Order Confirmation is personal to User. Therefore, User may not assign or transfer to any other person (whether a natural person or an organization of any kind) the license created by the Order Confirmation and these terms and conditions or any rights granted hereunder; provided, however, that User may assign such license in its entirety on written notice to CCC in the event of a transfer of all or substantially all of User's rights in the new material which includes the Work(s) licensed under this Service.

8.4 No amendment or waiver of any terms is binding unless set forth in writing and signed by the parties. The Rightsholder and CCC hereby object to any terms contained in any writing prepared by the User or its principals, employees, agents or affiliates and purporting to govern or otherwise relate to the licensing transaction described in the Order

Confirmation, which terms are in any way inconsistent with any terms set forth in the Order Confirmation and/or in these terms and conditions or CCC's standard operating procedures, whether such writing is prepared prior to, simultaneously with or subsequent to the Order Confirmation, and whether such writing appears on a copy of the Order Confirmation or in a separate instrument.

8.5 The licensing transaction described in the Order Confirmation document shall be governed by and construed under the law of the State of New York, USA, without regard to the principles thereof of conflicts of law. Any case, controversy, suit, action, or proceeding arising out of, in connection with, or related to such licensing transaction shall be brought, at CCC's sole discretion, in any federal or state court located in the County of New York, State of New York, USA, or in any federal or state court whose geographical jurisdiction covers the location of the Rightsholder set forth in the Order Confirmation. The parties expressly submit to the personal jurisdiction and venue of each such federal or state court.If you have any comments or questions about the Service or Copyright Clearance Center, please contact us at 978-750-8400 or send an e-mail to info@copyright.com.

v 1.1

Questions? customercare@copyright.com or +1-855-239-3415 (toll free in the US) or +1-978-646-2777.

Copyright agreement for Figure 1.6 in Section 1.2.2

JOHN WILEY AND SONS LICENSE TERMS AND CONDITIONS

Jan 21, 2018

This Agreement between Nathan Peterson ("You") and John Wiley and Sons ("John Wiley and Sons") consists of your license details and the terms and conditions provided by John Wiley and Sons and Copyright Clearance Center.

License Number	4271550722071
License date	Jan 17, 2018
Licensed Content Publisher	John Wiley and Sons
Licensed Content Publication	Wiley Books
Licensed Content Title	Fundamentals of Materials Science and Engineering: An Integrated Approach, 4th Edition
Licensed Content Author	David G. Rethwisch William D. Callister
Licensed Content Date	May 1, 2012
Licensed Content Pages	1
Type of Use	Dissertation/Thesis
Requestor type	University/Academic
Format	Print and electronic
Portion	Figure/table
Number of figures/tables	1
Original Wiley figure/table number(s)	Figure 7.12
Will you be translating?	No
Title of your thesis / dissertation	Measurement of Planar Fault Probabilities in Austempered Ductile Iron and 304L Stainless Steel
Expected completion date	May 2018
Expected size (number of pages)	60
Requestor Location	Nathan Peterson [redacted] Attn: Nathan Peterson
Publisher Tax ID	EU826007151
Total	**0.00 USD**
Terms and Conditions	

TERMS AND CONDITIONS

This copyrighted material is owned by or exclusively licensed to John Wiley & Sons, Inc. or one of its group companies (each a"Wiley Company") or handled on behalf of a society with which a Wiley Company has exclusive publishing rights in relation to a particular work (collectively "WILEY"). By clicking "accept" in connection with completing this licensing transaction, you agree that the following terms and conditions apply to this transaction (along with the billing and payment terms and conditions established by the Copyright Clearance Center Inc., ("CCC's Billing and Payment terms and conditions"), at the time that you opened your RightsLink account (these are available at any time at http://myaccount.copyright.com).

Terms and Conditions

- The materials you have requested permission to reproduce or reuse (the "Wiley Materials") are protected by copyright.

- You are hereby granted a personal, non-exclusive, non-sub licensable (on a stand-alone basis), non-transferable, worldwide, limited license to reproduce the Wiley Materials for the purpose specified in the licensing process. This license, **and any CONTENT (PDF or image file) purchased as part of your order,** is for a one-time use only and limited to any maximum distribution number specified in the license. The first instance of republication or reuse granted by this license must be completed within two years of the date of the grant of this license (although copies prepared before the end date may be distributed thereafter). The Wiley Materials shall not be used in any other manner or for any other purpose, beyond what is granted in the license. Permission is granted subject to an appropriate acknowledgement given to the author, title of the material/book/journal and the publisher. You shall also duplicate the copyright notice that appears in the Wiley publication in your use of the Wiley Material. Permission is also granted on the understanding that nowhere in the text is a previously published source acknowledged for all or part of this Wiley Material. Any third party content is expressly excluded from this permission.

- With respect to the Wiley Materials, all rights are reserved. Except as expressly granted by the terms of the license, no part of the Wiley Materials may be copied, modified, adapted (except for minor reformatting required by the new Publication), translated, reproduced, transferred or distributed, in any form or by any means, and no derivative works may be made based on the Wiley Materials without the prior permission of the respective copyright owner.**For STM Signatory Publishers clearing permission under the terms of the STM Permissions Guidelines only, the terms of the license are extended to include subsequent editions and for editions in other languages, provided such editions are for the work as a whole in situ and does not involve the separate exploitation of the permitted figures or extracts,** You may not alter, remove or suppress in any manner any copyright, trademark or other notices displayed by the Wiley Materials. You may not license, rent, sell, loan, lease, pledge, offer as security, transfer or assign the Wiley Materials on a stand-alone basis, or any of the rights granted to you hereunder to any other person.

- The Wiley Materials and all of the intellectual property rights therein shall at all times remain the exclusive property of John Wiley & Sons Inc, the Wiley Companies, or their respective licensors, and your interest therein is only that of having possession of and the right to reproduce the Wiley Materials pursuant to Section 2 herein during the continuance of this Agreement. You agree that you own no right, title or interest in or to the Wiley Materials or any of the intellectual property rights therein. You shall have no rights hereunder other than the license as provided for above in Section 2. No right, license or interest to any trademark, trade name, service mark or other branding ("Marks") of WILEY or its licensors is granted hereunder, and you agree that you shall not assert any such right, license or interest with respect thereto

- NEITHER WILEY NOR ITS LICENSORS MAKES ANY WARRANTY OR REPRESENTATION OF ANY KIND TO YOU OR ANY THIRD PARTY, EXPRESS, IMPLIED OR STATUTORY, WITH RESPECT TO THE MATERIALS OR THE ACCURACY OF ANY INFORMATION CONTAINED IN THE MATERIALS, INCLUDING, WITHOUT LIMITATION, ANY IMPLIED WARRANTY OF MERCHANTABILITY, ACCURACY, SATISFACTORY QUALITY, FITNESS FOR A PARTICULAR PURPOSE, USABILITY, INTEGRATION OR NON-INFRINGEMENT AND ALL SUCH WARRANTIES ARE HEREBY EXCLUDED BY WILEY AND ITS LICENSORS AND WAIVED BY YOU.

- WILEY shall have the right to terminate this Agreement immediately upon breach of this Agreement by you.

- You shall indemnify, defend and hold harmless WILEY, its Licensors and their respective directors, officers, agents and employees, from and against any actual or threatened claims, demands, causes of action or proceedings arising from any breach of this Agreement by you.

- IN NO EVENT SHALL WILEY OR ITS LICENSORS BE LIABLE TO YOU OR ANY OTHER PARTY OR ANY OTHER PERSON OR ENTITY FOR ANY SPECIAL, CONSEQUENTIAL, INCIDENTAL, INDIRECT, EXEMPLARY OR PUNITIVE DAMAGES, HOWEVER CAUSED, ARISING OUT OF OR IN CONNECTION WITH THE DOWNLOADING, PROVISIONING, VIEWING OR USE OF THE MATERIALS REGARDLESS OF THE FORM OF ACTION, WHETHER FOR BREACH OF CONTRACT, BREACH OF WARRANTY, TORT, NEGLIGENCE, INFRINGEMENT OR OTHERWISE (INCLUDING, WITHOUT LIMITATION, DAMAGES BASED ON LOSS OF PROFITS, DATA, FILES, USE, BUSINESS OPPORTUNITY OR CLAIMS OF THIRD PARTIES), AND WHETHER OR NOT THE PARTY HAS BEEN ADVISED OF THE POSSIBILITY OF SUCH DAMAGES. THIS LIMITATION SHALL APPLY NOTWITHSTANDING ANY FAILURE OF ESSENTIAL PURPOSE OF ANY LIMITED REMEDY PROVIDED HEREIN.

- Should any provision of this Agreement be held by a court of competent jurisdiction to be illegal, invalid, or unenforceable, that provision shall be deemed amended to achieve as nearly as possible the same economic effect as the original provision, and the legality, validity and enforceability of the remaining provisions of this Agreement shall not be affected or impaired thereby.

- The failure of either party to enforce any term or condition of this Agreement shall not constitute a waiver of either party's right to enforce each and every term and condition of this Agreement. No breach under this agreement shall be deemed waived or

excused by either party unless such waiver or consent is in writing signed by the party granting such waiver or consent. The waiver by or consent of a party to a breach of any provision of this Agreement shall not operate or be construed as a waiver of or consent to any other or subsequent breach by such other party.

- This Agreement may not be assigned (including by operation of law or otherwise) by you without WILEY's prior written consent.
- Any fee required for this permission shall be non-refundable after thirty (30) days from receipt by the CCC.
- These terms and conditions together with CCC's Billing and Payment terms and conditions (which are incorporated herein) form the entire agreement between you and WILEY concerning this licensing transaction and (in the absence of fraud) supersedes all prior agreements and representations of the parties, oral or written. This Agreement may not be amended except in writing signed by both parties. This Agreement shall be binding upon and inure to the benefit of the parties' successors, legal representatives, and authorized assigns.
- In the event of any conflict between your obligations established by these terms and conditions and those established by CCC's Billing and Payment terms and conditions, these terms and conditions shall prevail.
- WILEY expressly reserves all rights not specifically granted in the combination of (i) the license details provided by you and accepted in the course of this licensing transaction, (ii) these terms and conditions and (iii) CCC's Billing and Payment terms and conditions.
- This Agreement will be void if the Type of Use, Format, Circulation, or Requestor Type was misrepresented during the licensing process.
- This Agreement shall be governed by and construed in accordance with the laws of the State of New York, USA, without regards to such state's conflict of law rules. Any legal action, suit or proceeding arising out of or relating to these Terms and Conditions or the breach thereof shall be instituted in a court of competent jurisdiction in New York County in the State of New York in the United States of America and each party hereby consents and submits to the personal jurisdiction of such court, waives any objection to venue in such court and consents to service of process by registered or certified mail, return receipt requested, at the last known address of such party.

WILEY OPEN ACCESS TERMS AND CONDITIONS

Wiley Publishes Open Access Articles in fully Open Access Journals and in Subscription journals offering Online Open. Although most of the fully Open Access journals publish open access articles under the terms of the Creative Commons Attribution (CC BY) License only, the subscription journals and a few of the Open Access Journals offer a choice of Creative Commons Licenses. The license type is clearly identified on the article.

The Creative Commons Attribution License

The Creative Commons Attribution License (CC-BY) allows users to copy, distribute and transmit an article, adapt the article and make commercial use of the article. The CC-BY license permits commercial and non-

Creative Commons Attribution Non-Commercial License

The Creative Commons Attribution Non-Commercial (CC-BY-NC)License permits use, distribution and reproduction in any medium, provided the original work is properly cited and is not used for commercial purposes.(see below)

Creative Commons Attribution-Non-Commercial-NoDerivs License

The Creative Commons Attribution Non-Commercial-NoDerivs License (CC-BY-NC-ND) permits use, distribution and reproduction in any medium, provided the original work is properly cited, is not used for commercial purposes and no modifications or adaptations are made. (see below)

Use by commercial "for-profit" organizations

Use of Wiley Open Access articles for commercial, promotional, or marketing purposes requires further explicit permission from Wiley and will be subject to a fee.

Further details can be found on Wiley Online Library http://olabout.wiley.com/WileyCDA/Section/id-410895.html

Other Terms and Conditions:

v1.10 Last updated September 2015

Questions? customercare@copyright.com or +1-855-239-3415 (toll free in the US) or +1-978-646-2777.

Copyright agreement for Figure A.1 in Appendix A (pg. 53), Figure B.1 in Appendix B (pg. 57) and Figure C.1 in Appendix C (pg. 63)

Michigan Tech

Nate Peterson <[redacted]@mtu.edu>

Permission request / Warren: X-ray Diffraction

John Grafton <john.grafton@lsccom.com> Mon, Jan 22, 2018 at 11:15 AM
To: [redacted]@mtu.edu

Dear Mr. Peterson,
Thanks for your message. Permission granted to reproduce the three requested figures from Warren: **X-ray Diffraction** in your forthcoming thesis. All we request is credit to the Dover edition in any standard form.

Best regards,

John Grafton/Senior Editor
Dover publications, Inc,
1/22/2018

From: **Nate Peterson** <[redacted]@mtu.edu>
Date: Mon, Jan 22, 2018 at 10:34 AM
Subject: Reuse Copyright Request - For use in dissertation/thesis
To: rights@doverpublications.com

hello,

I'm working on completing at Master's thesis at Michigan Technological University and I'd like to request permission to reuse two figures from the following text:

X-ray Diffraction
B.E. Warren
ISBN-10: 0486663175

The three figures are:
Figure 13.14 on page 276
Figure 13.15 on Page 278
Figure 13.16 on Page 279

You may contact me at this email address or at my cell phone [redacted]

thank you,

- Nate Peterson